Re-interpretation of the Homogenized Constrained Mixture Theory within the plasticity framework and application to soft tissue growth and remodeling

Felipe Sempértegui[a], Stéphane Avril[a,1]

[a]*Mines Saint-Étienne, Univ Jean Monnet, INSERM, U 1059 Sainbiose, F - 42023, Saint-Étienne, France*

Abstract

The homogenized constrained mixture theory (H-CMT) is an attractive and efficient computational framework to simulate growth and remodeling (G&R) of soft tissues within finite deformations. It considers several prestressed constituents within a mixture and it enables their continuous individual mass removal and production to be taken into account. However, the referred theory was developed for specific mixtures, whose remodeling occurred on unidimensional constituents (fibers) only, while being embedded in an isotropic matrix. As the microstructure of soft tissues is generally more complex, we propose an extension of the H-CMT, which enables remodeling to occur on tridimensional constituents. This was achieved by manipulating the remodeling stress rate equation of the H-CMT. By rearranging the tensorial expression, it was possible to re-interpret its terms as variables of the classical plasticity theory and the resulting equation is a particular case of kinematic hardening. This interpretation, in turn, enables standard return mapping algorithms, which are classical in plasticity, to be quickly adapted to G&R problems. Therefore, not only we explore the intersection of both the H-CMT and the plasticity frameworks, but we also propose new algorithmic implementations of G&R that closely resemble those used in standard elasto-plastic problems. Applications to the simulation of G&R in anisotropic tissues such as arteries are eventually shown to demonstrate the capabilities of the new algorithms.

Keywords: plasticity, kinematic hardening, growth and remodeling, tissue engineered vascular graft

1. Introduction

The research field known as mechanobiology encompasses the study of growth and remodeling (G&R) in response to mechanical or chemical cues, through which biological tissues seek to restore or maintain a homeostatic state (Loerakker and Ristori, 2020), while its constituents are continuously produced or degraded. The study of G&R has grown substantially during the past years (Cyron and Humphrey, 2017) and researchers made efforts to develop adequate computational models, so as to support a deeper understanding of the undergoing phenomena.

Among these models, a significant number of them were developed on top of the noticeable constrained mixture theory (CMT) (Humphrey and Rajagopal, 2002). Such a framework was extensively used to predict the evolution of pathologies related to the aorta (Watton et al., 2004; Valentin et al., 2009; Cardamone et al., 2010) or other blood vessels (Ramachandra et al., 2017), while varying hemodynamic loads or simulating the effects of inflammation. The CMT was also used to elucidate questions about how a functional neo-tissue could be formed from a degrading Tissue-Engineered Vascular Graft (TEVG) (Khosravi et al., 2015; Miller et al., 2015; Szafron et al., 2019; Drews et al., 2020; Blum et al., 2022). These examples show that phenomenological models might support the development of several clinical applications, such as the prevention of aneurysmal diseases or the design of TEVGs.

Despite the continuing insights into G&R, the CMT remains computationally expensive (Latorre et al., 2022). It requires to store in memory all past configurations of every constituent within the mixture, as their stresses and mass evolutions are based on hereditary integrals. The main approach to circumvent this issue is to

Email addresses: f.sempertegui@emse.fr (Felipe Sempértegui), avril@emse.fr (Stéphane Avril)

[1]please, email this author

represent the simulated material with simplified geometries, such as cylinders. However, if one wishes to predict G&R on patient-specific geometries, memory storage will likely be a bottleneck. This, in turn, motivated the development of models that are cost effective (*i.e.*, "reduced models").

Cyron et al. (2016) proposed a reduced version of the CMT by homogenizing the elastic and inelastic deformation gradients in time. It is referred to as the H-CMT. Its key feature relies on assuming that the Cauchy stress rate "$\dot{\boldsymbol{\sigma}}$" can be defined via a mass-averaged Cauchy stress of all mass increments. From that rate expression in *tensor form*, Cyron et al. (2016) derived a *scalar* variant, which is appropriate to describe the remodeling of 1D-like materials only. For instance, Cyron et al. (2016) used Fung exponential (Fung, 1973; Holzapfel et al., 2000) strain energy density functions (SEDs) to test that *scalar* expression of remodeling. An explicit and ready-to-use equation was only presented for these unidimensional cases and, to our knowledge, no explicit framework was given about its original *tensor form*.

This reduced approach paved the way for the application of the H-CMT to more complex geometries. For instance, Mousavi and Avril (2017) and Mousavi et al. (2019) studied the development of aortic aneurysmal growth via the H-CMT, while using patient-specific data. In those studies, elastin was the only constituent of the mixture to be modeled as a tridimensional and isotropic solid, and it is assumed not to remodel. On the other hand, all other constituents suffer remodeling and are all represented as 1D Fung exponentials. As only the fibers undergo remodeling, Cyron et al. (2016) implemented the aforementioned *scalar*-rate equation, as there was no need to implement its *tensor* variant.

Another attempt to circumvent the computational costs of the classical CMT was the development of a mechanobiologically equilibrated CMT (ME-CMT) (Latorre and Humphrey, 2020a,b). Here, the hereditary integrals are transformed into rate expressions, while assuming that equilibrium occurs at a time that is much larger than the characteristic G&R time-scale.

Although being built under a more stringent assumption, it describes well the G&R problems cited above. For instance, Latorre and Humphrey (2018) studied an aortic aneurysm by locally varying the mass fractions of elastin, while Latorre et al. (2022) went further and used this reduced framework to predict G&R occurring in TEVGs.

The development of H-CMT & ME-CMT are important steps towards patient-specific simulations on irregular (patient-specific) geometries. However, numerical issues might still arise. For instance, such models could experience convergence issues, if (almost) no 3D material is cementing the aforementioned fibers within an element. Briefly, these instabilities might occur, as 1D fibers do not support shear. This leads to undesired high shear effects in the 3D materials, if the latter are almost absent within the mixture.

A logical solution to alleviate this problem is the inclusion of a 3D constituent in the model, so the material can support these shear effects. This 3D constituent could be isotropic and is implemented solely for numerical stability. Another alternative is the substitution of the unidimensional constituents to an equivalent 3D anisotropic material, such as a dispersed-like fiber proposed by Gasser et al. (2006). This material is a combination of an unidimensional component with an isotropic one.

In both cases, the inclusion of either an isotropic or an anisotropic material would require G&R to occur in the added material as well. If the H-CMT is the chosen approach to develop such a model, one requires to solve the stress rate equation of the H-CMT in its *tensor form*. To our best knowledge, the referred original tensor-like equation was not explicitly presented, as the implementation of its *scalar* variant was sufficient to predict remodeling of all cited problems (Cyron et al., 2016; Mousavi et al., 2019).

In the current paper, we propose a formal extension of the H-CMT that can address remodeling more globally, and in particular within 3D isotropic and anisotropic materials. For that, we modeled G&R as a variant of finite plasticity, as already suggested by Vignes and Papadopoulos (2010); Grillo et al. (2019); Soleimani (2019); Lamm et al. (2022). This enabled manipulating the H-CMT stress rate and re-interpreting it as a particular form of *kinematic hardening*. Not only both frameworks seemed to match well, but the resulting algorithm was able to generate results that were in good agreement with experimental data (Eichinger et al., 2020). Lastly, we also tested our algorithm on models containing anisotropic dispersed fibers.

2. Theory

2.1. Kinematics

We start from 2 assumptions that arise from the H-CMT and the CMT frameworks:

1. The studied solid mixture is composed of several constituents, each of them having a specific stress-free configuration,

2. The total deformation gradient $\mathbf{F}$ of the referred mixture can be decomposed into an elastic and an inelastic component.

Since all materials in this mixture deform together via the unified $\mathbf{F}$, the combination of the aforementioned assumptions can be expressed for every constituent "i" with

$$\mathbf{F} = \mathbf{F}^i_e \, \mathbf{F}^i_{gr}, \tag{1}$$

where $\mathbf{F}^i_e$ is the elastic deformation gradient, which generates the stresses; $\mathbf{F}^i_{gr}$ is the inelastic component; and the superscript "i" indicates a property or a variable of the constituent "i".

The inelastic term $\mathbf{F}^i_{gr}$ represents the G&R occurring within the mixture and it can be decomposed further into 2 additional components:

$$\mathbf{F}^i_{gr} = \mathbf{F}^i_r \, \mathbf{F}^i_g, \tag{2}$$

where $\mathbf{F}^i_r$ is associated with remodeling (*i.e.*, changes in the tissue's micro-structure) and $\mathbf{F}^i_g$ is related to a constituent's differential mass turnover.

In this work, it is assumed that the growth deformation $\mathbf{F}^i_g$ of a volume element is affected by the combined mass variations of all constituents. We assume that the growth deformation satisfies (Braeu et al., 2017)

$$\mathbf{F}^i_g = \mathbf{F}_g = \left(J_g - 1\right) \mathbf{N}^\perp \otimes \mathbf{N}^\perp + \mathbf{I}, \tag{3}$$

where $\mathbf{N}^\perp$ is a vector indicating the growth direction [for instance along the sample's thickness for a blood vessel (Braeu et al., 2017)], and

$$\begin{aligned} J_g &= \frac{\rho_0}{\rho_{0\,\mathrm{init}}}, \\ \rho_0 &= \sum \rho^i_0, \\ \rho_{0\,\mathrm{init}} &= \sum \rho^i_{0\,\mathrm{init}}, \end{aligned} \tag{4}$$

where ρ_0 and ρ^i_0 are the reference mass densities of the mixture and of a constituent "i" at current time, respectively; and the subscript "init" indicates densities being evaluated at the beginning of the G&R process (*i.e.*, at "$t = 0$").

Eqs. (1, 2, 3) can then be combined and recast as

$$\mathbf{F} = \mathbf{F}^i_e \, \mathbf{F}^i_r \, \mathbf{F}_g. \tag{5}$$

In this decomposition [Eq. (5)], we can establish proper configurations and they are schematically presented in Fig. 1. The inelastic deformations ($\mathbf{F}^i_r \, \mathbf{F}_g$) modify the material points from the reference configuration Γ_0 to the *intermediate remodeling configuration* $\bar{\Gamma}^i$. $\mathbf{F}^i_e$ is the deformation from the intermediate configuration to the current configuration Γ. We also define the *intermediate growth configuration* $\tilde{\Gamma}$ as the deformation of Γ_0 by the growth deformation $\mathbf{F}_g$ only.

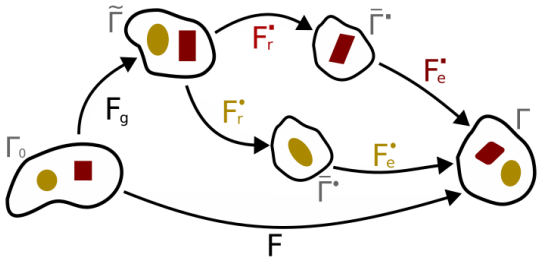

Figure 1: Multiplicative split used in the Homogenized Constrained Mixture Theory and related configurations. We show an example of a mixture with 2 constituents: constituent "◯" & constituent "□".

For a given state where all deformation gradients $\mathbf{F}$, $\mathbf{F}^i_e$, $\mathbf{F}^i_r$ and $\mathbf{F}_g$ are known, we wish to derive their increments for any material point. Relevant quantities for the increments of remodeling deformations are:

- the remodeling velocity gradient tensor

$$\bar{\mathbf{L}}^i_r = \dot{\mathbf{F}}^i_r \, \mathbf{F}^{i^{-1}}_r, \tag{6}$$

- the symmetric remodeling velocity gradient tensor

$$\bar{\mathbf{D}}^i_r = \mathrm{sym}\left[\bar{\mathbf{L}}^i_r\right], \tag{7}$$

- the rate of the right Cauchy-Green remodeling deformation tensor

$$\dot{\bar{\mathbf{C}}}^i_r = 2\mathbf{F}^{i^T}_r \, \bar{\mathbf{D}}^i_r \mathbf{F}^i_r. \tag{8}$$

The objective of our study is to extend the framework proposed by Cyron et al. (2016) from 1D materials to 3D isotropic and anisotropic constituents. It is done by defining a flow rule as in plasticity and with the help of Eqs. (6, 7, 8) [used in Sec. 2.5].

2.2. *Equilibrium & constitutive equations*

The quasi-static equilibrium of the mixture can be written as

$$\begin{aligned} \mathrm{DIV}\left(\mathbf{P}\right) + \rho_0 \mathbf{b}_0 &= \mathbf{0}, \\ \rho_0 &= \rho \left|\mathbf{F}\right|, \end{aligned} \tag{9}$$

where $\mathbf{P}$ is the 1$^{\mathrm{st}}$ Piola-Kirchhoff stress, $\mathbf{b}_0$ is the body force per unit reference mass and ρ is the current and unchanged total mass density.

The stress tensor $\mathbf{P}$ is derived from the total SED per unit reference volume ψ (i.e., $\mathbf{P} = \frac{\partial \psi}{\partial \mathbf{F}}$),

$$\psi = \sum \rho_0^i W^i, \tag{10}$$

being W^i a SED per unit reference mass of the constituent "i". In turn, the 2$^{\text{nd}}$ Piola-Kirchhoff stress of the mixture ($\mathbf{S}$) and of each constituent ($\mathbf{S}^i$) can be obtained such as

$$\begin{aligned} \mathbf{S} = 2\frac{\partial \psi}{\partial \mathbf{C}} = 2\sum \rho_0^i \frac{\partial W^i}{\partial \mathbf{C}} = \frac{1}{\rho_0}\sum \rho_0^i \mathbf{S}^i, \\ \mathbf{S}^i = 2\rho_0 \frac{\partial W^i}{\partial \mathbf{C}}. \end{aligned} \tag{11}$$

Finally, by using a push-forward operation, one can obtain the Cauchy stress $\boldsymbol{\sigma}^i$ of a constituent "i":

$$\boldsymbol{\sigma}^i = \frac{1}{|\mathbf{F}|}\mathbf{F}\mathbf{S}^i\mathbf{F}^T. \tag{12}$$

In this work, the variations of the stress $\boldsymbol{\sigma}^i$ [Eq. (12)] for a constituent "i" occur due to remodeling. As several new variables are introduced further, the superscripts "i" used so far are dropped from here onwards for the sake of clarity.

2.3. Intersecting H-CMT with plasticity

In the H-CMT (Cyron et al., 2016), it is assumed that remodeling occurs while the growth and the total deformation gradients are kept constant. Accordingly, the Cauchy stress rate of a single constituent "i" satisfies

$$\dot{\boldsymbol{\sigma}}|_{\mathbf{F},\mathbf{F}_g=const.} = -\left[\frac{\dot{\rho}_{0+}}{\rho_0}\right]\left[\boldsymbol{\sigma} - \boldsymbol{\sigma}_{pre}\right], \tag{13}$$

where $\boldsymbol{\sigma}$ is the current Cauchy stress, $\boldsymbol{\sigma}_{pre}$ is the preferred or homeostatic stress, and $\dot{\rho}_{0+}$ is referred to as the deposition rate.

Cyron et al. (2016) also assumed that the rate of mass removal ($\dot{\rho}_{0-}$) is governed by a Poisson process, such as

$$\dot{\rho}_{0-} = -\frac{\rho_0}{T}, \tag{14}$$

where T is the exponential survival function or the averaged turnover time. Hence, the total rate of the reference density is

$$\dot{\rho}_0 = \dot{\rho}_{0+} + \dot{\rho}_{0-}. \tag{15}$$

From here, we combine 4 features that are commonly implemented in finite plasticity or modeled biological tissues:

1. Discrete time steps, denoted t_n, are introduced and an approximate solution of Eq. (13) is computed with the backward (implicit) Euler scheme (Bonet and Wood, 1997; Hashiguchi and Yamakawa, 2012; de Souza Neto et al., 2011; Simo, 1992),
2. The remodeling tensor $\mathbf{F}_r^i$ is incompressible (Cyron et al., 2016; Braeu et al., 2017),
3. The SED of the 3D material can be split into a volumetric and a deviatoric contribution,
4. It is assumed that only the isochoric component of the preferred stress $\boldsymbol{\sigma}_{pre}$ triggers remodeling in the tissue.

In this section, we only present the final equation that can be established from the aforementioned points. More details can be found in Appendix A. Here, we recast Eq. (13) as

$$\hat{\boldsymbol{\sigma}}'(t_{n+1}) = \boldsymbol{\sigma}'(t_{n+1}) - \boldsymbol{\sigma}'_r(t_{n+1}) = \mathbf{0}, \tag{16}$$

where $\hat{\boldsymbol{\sigma}}$ is the relative stress, $\boldsymbol{\sigma}_r$ is the *backstress* and the superscript "$\prime$" is an indication that only the deviatoric term should be taken into account. In turn, the *backstress* can be represented as

$$\boldsymbol{\sigma}_r(t_{n+1}) = \left[\left(\frac{\triangle\, \rho_{0+}}{\triangle\, \rho_{0+} + \rho_0}\right)_{k+1} \boldsymbol{\sigma}_{pre} + \left(\frac{\rho_0}{\triangle\, \rho_{0+} + \rho_0}\right)_{k+1} \boldsymbol{\sigma}(t_n)\right], \tag{17}$$

where the tensor $\boldsymbol{\sigma}(t_n)$ indicates a fictitious stress state *prior* to remodeling but *after* growth, the subscript "$k+1$" represents the updated density quantities related to the phenomena of growth *prior* to remodeling. $\triangle\rho_{0+}$ is the incremental equivalent of $\dot{\rho}_{0+}$ and it is also discretized with the same time-integration scheme, which results in

$$(\triangle\rho_{0+})_{k+1} = \begin{cases} \left(1 + \frac{\triangle t}{T}\right)\rho_{0_{k+1}} - \rho_{0_k}, & \text{if } \triangle\rho_{0+} \geq 0, \\ 0, & \text{otherwise,} \end{cases} \tag{18}$$

where ρ_{0_k} is the reference density of the material *before* growth, and $\triangle t$ is the time increment (*i.e.*, $\triangle t = t_{n+1} - t_n$).

By introducing the Kirchhoff stresses $\boldsymbol{\tau} = J\boldsymbol{\sigma}$ (more commonly used in problems involving incompressible plasticity), we recast Eq. (16) into

$$\hat{\boldsymbol{\tau}}' = \boldsymbol{\tau}' - \boldsymbol{\tau}'_r = \mathbf{0}. \tag{19}$$

As $\hat{\boldsymbol{\tau}}'$ is a null tensor, all meaningful deviatoric invariants are zero as well (i.e., $J_2 = J_3 = 0$). In agreement with standards in plasticity, we chose J_2 as the meaningful scalar stress equivalent and we rewrote Eq. (19) such as

$$f = \frac{1}{2}\hat{\boldsymbol{\tau}}' : \hat{\boldsymbol{\tau}}' = 0, \tag{20}$$

where f is a scalar function which can be re-interpreted as a *yield criterion* in plasticity and it sets the basis to establish a flow rule providing the remodeling deformation rates of Eq. (13).

2.4. Comparing the H-CMT with the plasticity framework

2.4.1. Similarities

We established a bridge between the H-CMT (Cyron et al., 2016) and classical plasticity through the "f" scalar function in Eq. (20), which can be interpreted as a *von Mises yield criterion* with *kinematic hardening*. The *backstress* tensor $\boldsymbol{\tau}_r$ is the variable responsible for that hardening effect. It triggers remodeling to occur in the material.

Re-interpreting the H-CMT framework as a kinematic hardening problem is in perfect agreement with the work of Cyron and Aydin (2017), who proposed that the total energy of a material undergoing remodeling could be split into an elastic (ψ_e^c) and a remodeling energy (ψ_r^c), such that

$$\psi^c(\mathbf{F}_e, \mathbf{F}_r) = \psi_e^c(\mathbf{F}_e) + \psi_r^c(\mathbf{F}_r). \tag{21}$$

Feeding the Clausius-Duhem inequality with Eq. (21) naturally leads to kinematic hardening. Moreover, that procedure also shows that the current stress $\boldsymbol{\sigma}$ emerges from the elastic SED ψ_e^c, whereas the backstress $\boldsymbol{\sigma}_r$ emerges from its inelastic counterpart (ψ_r^c).

2.4.2. Differences

In spite of the aforementioned similarities, Eq. (20) is different from standard *kinematic hardening*. A typical yield criterion of that type would be written such as (Hashiguchi and Yamakawa, 2012; de Souza Neto et al., 2011):

$$f_p = \sqrt{\frac{3}{2}\hat{\boldsymbol{\tau}}' : \hat{\boldsymbol{\tau}}'} - \tau_0 \leq 0, \qquad \begin{matrix}\text{elastic, if } f_p < 0 \\ \text{plastic, if } f_p = 0\end{matrix} \tag{22}$$

However, in Eq. (20), $\tau_0 = 0$, or in other words, the yield criterion f is always null. This singularity reduces our *von Mises* "circle" (defining the *elastic domain*) to a "dot". As a consequence, the backstress $\boldsymbol{\tau}_r$ and the current stress $\boldsymbol{\tau}$ are always identical.

Another aspect of Eq. (20) is its applicability on anisotropic materials. It is well known that yield surfaces of such materials are usually defined with extra coefficients or with exotic combinations of "J_2" and "J_3" (Lou and Yoon, 2017). However, since both invariants are null in Eq. (19), equations containing both invariants would lead us to expressions that are also null. This feature can be interpreted geometrically in the stress space: As an elastic domain is not present in Eq. (20), any formulation (i.e., the classical *von Mises* "circle" or a complex anisotropic yield function) will be reduced to a "dot".

Another key difference is related to how the backstress is obtained in both frameworks. In standard plasticity, the backstress is traditionally obtained from a predefined inelastic SED [as shown in Eq. (21)]. In the H-CMT framework, there is no explicit expression and the backstress tensor is recovered from stress rate expressions given in Eq. (13) instead.

2.5. Deriving remodeling deformation rates

Following the notation of Hashiguchi and Yamakawa (2012), we introduce Mandel and Eshelby-like stresses, so as to describe the yield criterion such as

$$f = \frac{1}{2}\hat{\boldsymbol{\tau}}' : \hat{\boldsymbol{\tau}}' = \frac{1}{2}\hat{\bar{\mathbf{M}}}' : \hat{\bar{\mathbf{M}}}'^T = \frac{1}{2}\hat{\tilde{\mathbf{M}}}' : \hat{\tilde{\mathbf{M}}}'^T = 0, \tag{23}$$

where $\hat{\bar{\mathbf{M}}}$ and $\hat{\tilde{\mathbf{M}}}$ represent the relative Mandel stress (configuration $\bar{\Gamma}$) and Eshelby-like stress (configuration $\tilde{\Gamma}$), respectively, such as

$$\begin{aligned}\hat{\bar{\mathbf{M}}} &= \mathbf{F}_e^T\, \hat{\boldsymbol{\tau}}\, \mathbf{F}_e^{-T}, \\ \hat{\tilde{\mathbf{M}}} &= \left(\mathbf{F}\mathbf{F}_g^{-1}\right)^T \hat{\boldsymbol{\tau}} \left(\mathbf{F}\mathbf{F}_g^{-1}\right)^{-T}.\end{aligned} \tag{24}$$

We can now define the direction of a plastic flow rule with a flow vector $\bar{\mathbf{N}}$, while considering that the stress-like tensors in Eq. (23) might not be isotropic. To that end, we use the widely assumed *spinless* & *isoclinic* configuration $\bar{\Gamma}$ (Gurtin et al., 2010; Hashiguchi and Yamakawa, 2012; Latorre and Montans, 2018; Grillo et al., 2019; Hashiguchi, 2019; Yamakawa et al., 2021). By also defining it to be of the associative type, it follows that

$$\bar{\mathbf{N}} = \operatorname{sym}\left[\frac{\partial f}{\partial \bar{\mathbf{M}}}\right] \Big/ \left\| \operatorname{sym}\left[\frac{\partial f}{\partial \bar{\mathbf{M}}}\right] \right\|, \tag{25}$$

where $\bar{\mathbf{M}}$ is the Mandel stress.

With the aforementioned assumptions, $\operatorname{skew}[\bar{\mathbf{L}}_r] = \mathbf{0}$ and the remodeling velocity tensor is symmetric:

$$\bar{\mathbf{L}}_r = \bar{\mathbf{D}}_r = \dot{\lambda}\bar{\mathbf{N}}, \tag{26}$$

where $\dot{\lambda}$ is the plastic multiplier rate.

By performing a pull-back operation of Eq. (26) to the configuration $\tilde{\Gamma}$,

$$\dot{\tilde{\mathbf{C}}}_r = 2\sqrt{2}\,\dot{\lambda}\frac{\mathrm{sym}\left[\left(\frac{\partial f}{\partial \tilde{\mathbf{M}}}\right)^T \mathbf{C}_r\right]}{\sqrt{\left[\mathbf{C}_r \frac{\partial f}{\partial \tilde{\mathbf{M}}}\mathbf{C}_r^{-1}\right] : \left(\frac{\partial f}{\partial \tilde{\mathbf{M}}}\right) + \left(\frac{\partial f}{\partial \tilde{\mathbf{M}}}\right) : \left(\frac{\partial f}{\partial \tilde{\mathbf{M}}}\right)^T}} \tag{27}$$

where $\mathbf{C}_r$ is the right Cauchy-Green tensor $\left(\mathbf{C}_r = \mathbf{F}_r^T\mathbf{F}_r\right)$.

Lastly, we use the well-known exponential time-integration scheme (Vladimirov et al., 2008; Simo, 1992; Hashiguchi and Yamakawa, 2012; Yamakawa et al., 2021), ensuring plastic incompressibility and we obtain

$$\begin{aligned}
&\mathbf{C}_r(t_{n+1}) = [\mathbf{Q}(t_{n+1})]\ \mathbf{C}_r(t_n)\ [\mathbf{Q}(t_{n+1})]^T\,,\\
&\mathbf{Q} = \exp[\mathbf{Z}]\\
&\mathbf{Z} = \sqrt{2}\triangle\lambda\frac{\hat{\tilde{\mathbf{M}}}'}{\sqrt{\left[\mathbf{C}_r^{-1}\hat{\tilde{\mathbf{M}}}'\mathbf{C}_r\right] : \hat{\tilde{\mathbf{M}}}' + \hat{\tilde{\mathbf{M}}}' : \hat{\tilde{\mathbf{M}}}'^T}}.
\end{aligned} \tag{28}$$

where $\triangle\lambda$ is the incremental plastic multiplier $\triangle\lambda = \triangle t\,\dot{\lambda}$.

3. Methods

3.1. Algorithmic implementations

This section is focused on the algorithmic implementation of the theory exposed in the previous section. We choose the Newton-Raphson Method to solve the system of nonlinear (and incremental) equations, as it is standard in plasticity. We developed algorithms for 3 specific applications:

1. **Remodeling with prescribed growth:** The simplest of all cases are those where the variation of reference mass density is given. For instance, Drews et al. (2020) uses an analytical function to describe the mass evolution related to inflammation in a tissue. For this type of problem, the corresponding "ρ_0" can be directly assigned into the algorithm at each time increment.
2. **Stress-mediated G&R:** It is acknowledged in mechanobiology that mass degradation or deposition are stress dependent (Mousavi et al., 2019; Ramachandra et al., 2017). Therefore, an extra expression that relates mass variations and stresses should be added to the system of equations.
3. **Mixture:** Aforementioned approaches deal only with materials that are modeled with a single SED. However, mixtures is widely used in soft tissue biomechanics. Therefore, we present possible implementations of this framework in the context of a composite containing 2 isotropic constituents undergoing G&R.

3.2. Remodeling with prescribed growth

Only Eqs. (23, 28) should be solved if the reference mass densities ρ_{0_k} and $\rho_{0_{k+1}}$ are known [see Eqs. (17, 18)].

Moreover, due to the similarities between the H-CMT and kinematic hardening [see Sec. 2.4.1], Eqs. (23, 28) can be easily adapted to already exisiting codes related to plasticity. Since the Newton-Raphson Method is used in this work, these expressions are rewritten as residuals:

$$\begin{aligned}
&\mathbf{R}_{\mathbf{C}r} = \mathbf{C}_r^{n+1} - \mathbf{Q}\mathbf{C}_r^n\mathbf{Q}^T = \mathbf{0},\\
&R_f = f = \frac{1}{2}\hat{\tilde{\mathbf{M}}}' : \hat{\tilde{\mathbf{M}}}'^T = 0.
\end{aligned} \tag{29}$$

As $\mathbf{C}_r$ is symmetric, it is possible to use the Voigt notation and $\mathbf{R}_{\mathbf{C}r}$ can be transformed into a vector with 6 components. We symbolically represent and group the residuals' elements of $\mathbf{R}_{\mathbf{C}_r}$ and R_f together in a vector $\mathbf{Y}_{PG}$. The same procedure is performed on $\mathbf{C}_r$ and $\triangle\lambda$ which are gathered in vector $\mathbf{X}_{PG}$:

$$\mathbf{Y}_{PG} = \begin{Bmatrix}\mathbf{R}_{\mathbf{C}_r}\\ R_f\end{Bmatrix}_{7x1}, \quad \mathbf{X}_{PG} = \begin{Bmatrix}\mathbf{C}_r\\ \triangle\lambda\end{Bmatrix}_{7x1}, \tag{30}$$

where the "*PG*" subscript means that a "Prescribed Growth" problem is considered here.

Linearization is achieved by introducing a Jacobian tensor $\mathbf{J}_{PG}$ in Voigt notation and a corrector for $\mathbf{X}_{PG}$ (defined here as $\triangle\mathbf{X}_{PG}$), such as

$$\begin{aligned}
&\mathbf{J}_{PG}\ *\triangle\mathbf{X}_{PG} = -\mathbf{Y}_{PG},\\
&\mathbf{J}_{PG} = \begin{bmatrix}\frac{\partial\mathbf{R}_{\mathbf{C}_r}}{\partial\mathbf{C}_r} & \frac{\partial\mathbf{R}_{\mathbf{C}_r}}{\partial\triangle\lambda}\\ \frac{\partial R_f}{\partial\mathbf{C}_r} & \frac{\partial R_f}{\partial\triangle\lambda}\end{bmatrix}_{7x7}.
\end{aligned} \tag{31}$$

Each individual derivative of $\mathbf{J}_{PG}$ in Eq. (31) can be found in Appendix B.

3.3. Stress-mediated G&R

In the previous section we assumed that the mass density rates are known prior to remodeling. However, mass density rates may evolve as functions of stresses and deformations (Ramachandra et al., 2015; Braeu et al., 2017; Ghavamian et al., 2020; Drews et al., 2020). For instance, Ghavamian et al. (2020) postulated that the degradation of uniaxial fibers depends on the I_4 pseudo-invariant and Drews et al. (2020) proposed a mass deposition rate based on the stresses. More generally, we may describe the rate of reference mass density such as

$$\dot{\rho}_0 \equiv \dot{\rho}_0\left(\boldsymbol{\sigma}, \boldsymbol{\sigma}_{pre}, \mathbf{F}_e, \mathbf{F}_h\right). \tag{32}$$

Table 1: Test cases to demonstrate the coupling of Jacobian matrices

	Case 1	Case 2
material a	PG [Eq. (31)]	GR [Eq. (35)]
material b	GR [Eq. (35)]	GR [Eq. (35)]

The mass turnover is not known beforehand and growth should be coupled with remodeling as an additional algebraic equation to complete Eq. (29). By applying the backward Euler method to Eq. (32) and transforming it into an a residual expression, we obtain

$$R_{\rho_0} = \rho_{0_{k+1}} - \rho_{0_k} - \triangle t\, \dot{\rho}_{0_{k+1}} = 0. \tag{33}$$

This residual and the updated variable "ρ_0" are then included in the vectors introduced in Eq. (30). The updated expression is

$$\mathbf{Y}_{GR} = \begin{Bmatrix} \mathbf{R}_{\mathbf{C}_r} \\ R_f \\ R_{\rho_0} \end{Bmatrix}_{8x1}, \quad \mathbf{X}_{GR} = \begin{Bmatrix} \mathbf{C}_r \\ \triangle\lambda \\ \rho_0 \end{Bmatrix}_{8x1}, \tag{34}$$

where the "*GR*" subscript means that a "Growth & Remodeling" problem is considered here.

The Newton-Raphson algorithm for G&R becomes

$$\mathbf{J}_{GR} * \triangle\mathbf{X}_{GR} = -\mathbf{Y}_{GR},$$
$$\mathbf{J}_{GR} = \begin{bmatrix} \frac{\partial \mathbf{R}_{\mathbf{C}_r}}{\partial \mathbf{C}_r} & \frac{\partial \mathbf{R}_{\mathbf{C}_r}}{\partial \triangle\lambda} & \frac{\partial \mathbf{R}_{\mathbf{C}_r}}{\partial \rho_0} \\ \frac{\partial R_f}{\partial \mathbf{C}_r} & \frac{\partial R_f}{\partial \triangle\lambda} & \frac{\partial R_f}{\partial \rho_0} \\ \frac{\partial R_{\rho_0}}{\partial \mathbf{C}_r} & \frac{\partial R_{\rho_0}}{\partial \triangle\lambda} & \frac{\partial R_{\rho_0}}{\partial \rho_0} \end{bmatrix}_{8x8}. \tag{35}$$

Each additional derivative of $\mathbf{J}_{GR}$ in Eq. (35) can be found in Appendix D.

3.4. Mixture

Eqs. (31, 35) only deal with a single SED. In this section, we show an example involving 2 materials. Each material should be implemented with either Eqs. (31) or (35) and we considered 2 cases as reported in Tab. 1.

"Material a" might affect the remodeling of "material b", and vice versa, via the growth deformation gradient $\mathbf{F}_g$. As shown in Eq. (3), this tensor evolves w.r.t. to the mass densities of *all* constituents of the mixture. Therefore, coupling between the 2 materials should be explicitly defined in the final Jacobian matrix.

For "Case 1", the updated mass density ρ_0 from the "material b" should affect the remodeling of "material a" via a sub-matrix $\mathbf{J}_{GR\rightarrow PG}$:

$$\begin{bmatrix} \mathbf{J}_{PG} & \mathbf{J}_{GR\rightarrow PG} \\ \mathbf{0} & \mathbf{J}_{GR} \end{bmatrix} * \triangle \begin{Bmatrix} \mathbf{X}_{PG} \\ \mathbf{X}_{GR} \end{Bmatrix} = - \begin{Bmatrix} \mathbf{Y}_{PG} \\ \mathbf{Y}_{GR} \end{Bmatrix}. \tag{36}$$

The detailed expressions of $\mathbf{J}_{GR\rightarrow PG}$ are given in Appendix C.

For "Case 2", the mass densities of one material interferes with the other. Hence, 2 sub-matrices should be included in the global Jacobian matrix, which are named $\mathbf{J}_{GR\,a\rightarrow GR\,b}$ and $\mathbf{J}_{GR\,b\rightarrow GR\,a}$, yielding

$$\begin{bmatrix} \mathbf{J}_{GR\,a} & \mathbf{J}_{GR\,b\rightarrow GR\,a} \\ \mathbf{J}_{GR\,a\rightarrow GR\,b} & \mathbf{J}_{GR\,b} \end{bmatrix} * \triangle \begin{Bmatrix} \mathbf{X}_{GR\,a} \\ \mathbf{X}_{GR\,b} \end{Bmatrix} = - \begin{Bmatrix} \mathbf{Y}_{GR\,a} \\ \mathbf{Y}_{GR\,b} \end{Bmatrix}. \tag{37}$$

Each derivative in Eq. (37) can be found in Appendix E.

The sub-matrices have different dimensions and elements depending on how remodeling is defined for each constituent, as they can be ruled by either the "PG" case or the "GR" one. Fig. 2 illustrates how the elements of the global Jacobian matrices shown in Eqs. (36, 37) are arranged.

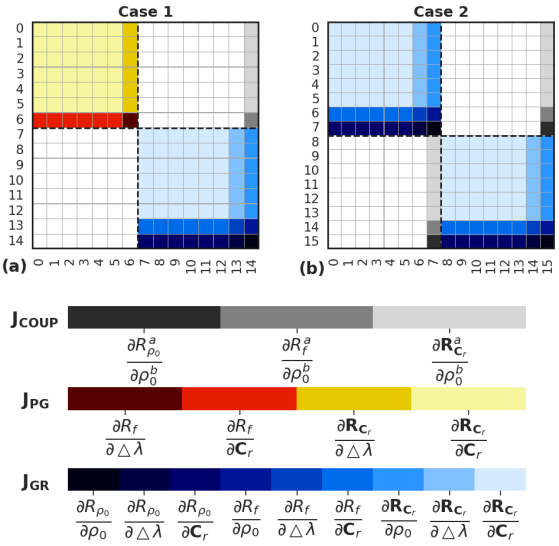

Figure 2: raphical illustration of the global Jacobian matrices of "case 1" [Eq. (36)] and "case 2" [Eq. (37)].

It shows that coupling effects between 2 3D constituents only results from the variations of their individual mass densities. The coupling terms are the column-like arrays in both global matrices, which correspond to partial derivatives w.r.t. ρ_0.

4. Numerical examples

The stress updating algorithms shown in Eqs. (31, 35, 36, 37) were incorporated in an in-house FEM code and the consistent tangent modulus was computed

by means of the perturbation technique (Simo, 1992; Miehe, 1996). For the examples in Secs. 4.1 & 4.2, we chose the Nearly Incompressible Neo-Hookean material to represent the elastic response of isotropic constituents. It can be formulated such as

$$\begin{aligned}\hat{\psi}_e^e &= \frac{\mu}{2}\left[\hat{I}_1 - 3\right],\\ U_e^e &= \frac{\Lambda^e}{2}\left[I_3^e - 1\right]^2,\\ I_3^e &= \sqrt{|\mathbf{b}_e|},\\ \hat{I}_1 &= \left[I_3^e\right]^{-\frac{2}{3}}\left[\mathbf{b}_e : \mathbf{I}\right],\end{aligned} \tag{38}$$

where μ and κ are material constantsand $\mathbf{b}_e$ is the elastic left Cauchy-Green tensor $\left(\mathbf{b}_e = \mathbf{F}_e\mathbf{F}_e^T\right)$.

Naturally, we chose the same SED to represent the isochoric preferred stress, which is computed from a preferred homeostatic stretch tensor $\mathbf{F}_h$ such as,

$$\begin{aligned}\boldsymbol{\tau}'_{pre} &= \mathbf{R}\boldsymbol{\tau}'_h\mathbf{R}^T,\\ \boldsymbol{\tau}'_h &= \mu\, I_3^{h\,-2/3}\left[\mathbf{b}_h - \frac{1}{3}I_1^h\mathbf{I}\right],\\ I_3^h &= \sqrt{|\mathbf{b}_h|},\\ I_1^h &= \left[I_3^h\right]^{-\frac{2}{3}}\left[\mathbf{b}_h : \mathbf{I}\right],\\ \mathbf{b}_h &= \mathbf{F}_h\mathbf{F}_h^T.\end{aligned} \tag{39}$$

As for the example in Sec. 4.3, we implemented an anisotropic material, which is suitable for modeling dispersed collagen fibers (Gasser et al., 2006).

4.1. Remodeling with prescribed growth

4.1.1. Proof-of-concept

The first example is an implementation of Eq. (31), where the rate of mass deposition is equal to that of degradation. For that, we enforce $\dot{\rho}_{0+} = \dot{\rho}_{0-}$ and, consequently, $\dot{\rho}_0 = 0$. Fig. 3 shows the simulated element, which is constrained at all facets with the exception of the top surface (this also serves for the numerical example of next subsection).

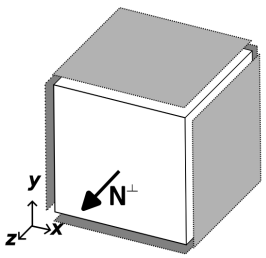

Figure 3: Constrained geometry. All gray facets are constrained. The only unconstrained surface is the frontal one. The normal direction of that facet is defined to be the growth direction $\mathbf{N}^{\perp}$ [Eq. (3)].

The material is set to be stress-free at the start of the simulation, while the preferred deformation state $\mathbf{F}_h$ is set to be $\mathbf{F}_h = \mathrm{diag}\left[\lambda, \frac{1}{\sqrt{\lambda}}, \frac{1}{\sqrt{\lambda}}\right]$. Tensor $\mathbf{F}_h$ is given to Eq. (39), which, in turn, provides the algorithm with $\boldsymbol{\tau}'_{pre}$. Then, the internal stresses of the material develop from a stress-free state towards $\boldsymbol{\tau}'_{pre}$ as the simulation progresses.

Fig. 4 (a) shows the internal stresses of the element presented in Fig. 3. As expected, the isochoric components of the stresses undergo remodeling, so as to develop the internal stresses until eventually reaching $\boldsymbol{\tau}'_{pre}$.

This evolution can also be seen in the stress-space from the deviatoric plane [Fig. 4 (b)]. The stress tensor starts at the axes origin [$\boldsymbol{\sigma}(t = 0)$] and it approaches the prestress $\boldsymbol{\sigma}_{pre}$. In the same figure, we also depict the yield surface (as explained before, it reduces to a dot as the yield surface's radius is actually null).

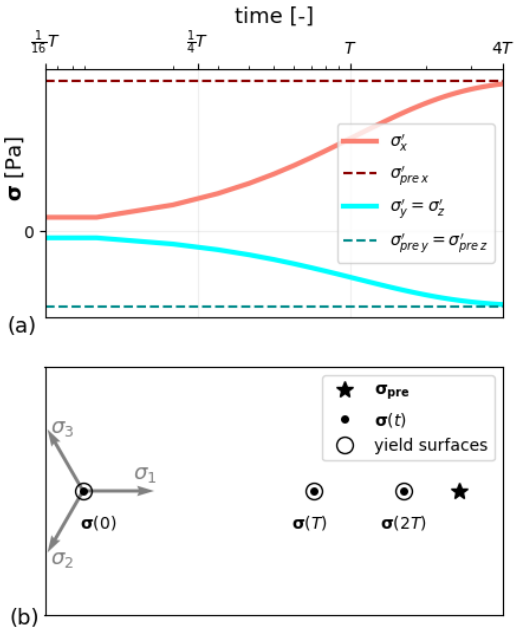

Figure 4: (a): Evolution of the isochoric Cauchy stress components. (b): Stresses in the stress-space and viewed from the deviatoric plane.

4.1.2. Comparison against experimental data

We also used Eq. (31) to reproduce experimental data. Eichinger et al. (2020) measured the tension produced by constrained cell-seeded collagen in uniaxial and biaxial settings, showing that the cells tend to establish and maintain a preferred (homeostatic) tension.

In the right-hand side of Fig. 5, we depict cell-seeded

collagen elements. The regions where they are constrained and where the tension was measured is represented by gray facets. In the left-hand side of the same figure, one can see that the measured tension on those facets stabilizes to a certain homeostatic tension.

In another experiment, Eichinger et al. (2020) inhibited cell proliferation. This corresponds to a case, where the mass density remains approximately constant ($\dot{\rho}_0 \approx 0$). These conditions allowed us to compare the "PG" algorithm [Eq. (31)] to their findings.

Fig. 5 shows that the results predicted by our algorithm are in very good agreement with the experimental measurements. While 2 mass turnovers were necessary to mimic the experimental data in Figs. 5 (a) and (c); only one was sufficient for Fig. 5 (b).

Particular attention was paid to the comparison shown in Fig. 5 (c). That experiment starts after an initial stretch of 1.8% along the x-direction and the tension normal to the yz plane is pronounced at the start of the experiment. Due to the in-plane coupling, the tension along the coordinate y is also non-zero, even though the values are less prominent. Nevertheless, our predicted stress evolution along both directions were still in very good agreement with the experiments.

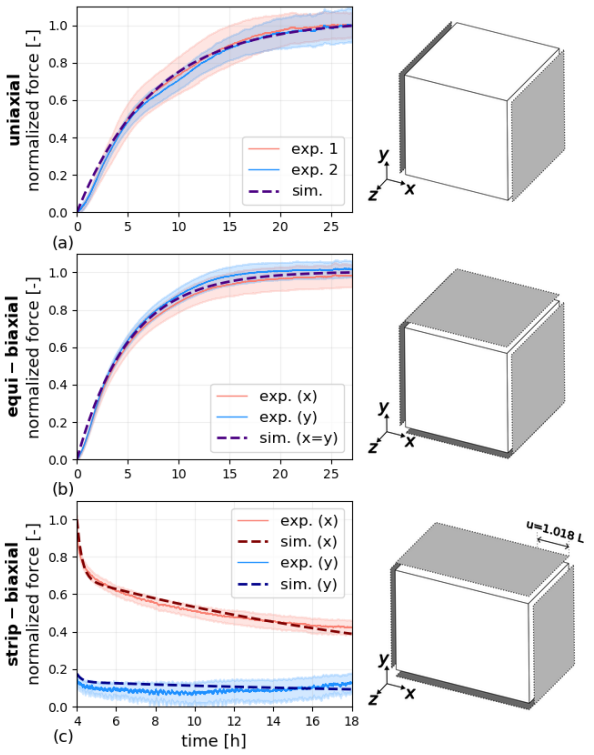

Figure 5: (a) Measurements performed in a uniaxial setting. Eq. (31) was applied on a isotropic material with 2 mass turnover rates: T_1=7 hours ($\phi_1 = 50\%$) and T_2=8 hours ($\phi_2 = 50\%$). In order to reproduce the uniaxial protocol, $\mathbf{F}_h$ was set to be diag$\left[\lambda, \frac{1}{\sqrt{\lambda}}, \frac{1}{\sqrt{\lambda}}\right]$. (b) Measurements of the equi-biaxial setting. A single mass turnover rate of T=5 hours was sufficient to fit our simulated data to the experiments. Here, $\mathbf{F}_h$ was set to be diag$\left[\lambda, \lambda, \frac{1}{\lambda^2}\right]$. (c) Strip-biaxial protocol after applying an initial stretch of $\lambda_i = 1.018$ to the cell-seeded collagen. A short mass turnover rate of T_1=0.21 hours ($\phi_1 = 33\%$) and another of T_2 =21 hours ($\phi = 67\%$) provided us with the simulated data shown in the graph. $\mathbf{F}_h$ was set to be the same as in (b). Eichinger et al. (2020) authorized the authors to expose their experimental data in this work.

4.2. *Stress-mediated G&R*

Here, the model shown in Fig. 3 was used to test the algorithm of Eq. (35). The top facet was unconstrained and the z coordinate was set to be the direction of growth, such that $\mathbf{N}^{\perp} = [0, 0, 1]$ in Eq. (3). The density rate expression in Appendix J was used in this example and it was set to reproduce 2 phenomena:

1. In the first numerical experiment, there is more deposition than degradation of mass, *i.e.*, $\dot{\rho}_0 > 0$.
2. In the second numerical experiment, degradation was more pronounced, with $\dot{\rho}_0 < 0$.

In both cases, the material was stress-free at the beginning of the simulation.

The evolution of a stress component is shown for both simulations in Fig. 6. It can be noted that internal stresses converge towards the preferred stress. The difference between the 2 numerical experiments is the time required for the convergence.

In the case where the deposition dominates ($\dot{\rho}_0 > 0$), the isochoric stress and $\boldsymbol{\sigma}'_{pre}$ are practically equal at $t = 4T$. However, the other case shows a slower increase of the stresses towards the homeostatic value.

These results are physically consistent. The higher the rate of mass deposition, the sooner the average stress within a given volume will reach $\boldsymbol{\sigma}'_{pre}$. Conversely, the average stress would evolve slower if lower quantities of mass deposition were prescribed, which was the case of the second experiment ($\dot{\rho}_0 < 0$).

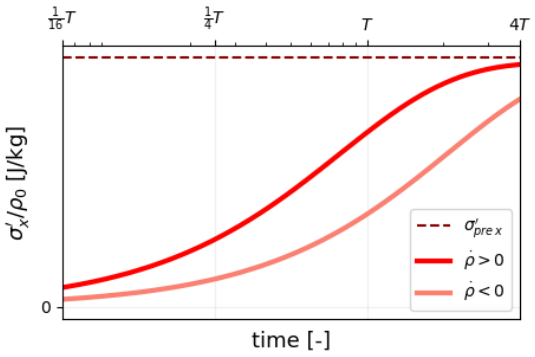

Figure 6: Evolution of the Cauchy stress under a more pronounced deposition ($\dot{\rho}_0 > 0$) and degradation ($\dot{\rho}_0 < 0$)

4.3. Mixture with Anisotropic Constituents

In this section, we present an implementation of [Eqs. (36, 37)] on mixtures, while taking into account the presence of anisotropic constituents. The test model is shown in Fig. 7 and it represents a tissue strip of arterial walls (Horvat et al., 2021). This model is composed of 3 constituents: 2 families of (anisotropic) dispersed fibers (Gasser et al., 2006) and an isotropic elastin matrix.

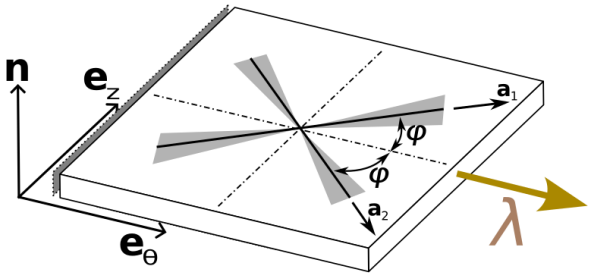

Figure 7: Model of a tissue representing a strip of an arterial wall. This model is composed of an elastin matrix (shown in white) and 2 dispersed fiber families (Gasser et al., 2006). The direction of these fibers are shown as black lines and their dispersion are represented with the color gray. The vectors $\mathbf{n}$, $\mathbf{e}_z$, $\mathbf{e}_\theta$ represent the current configuration of the normal, axial and circumferential directions of the arterial wall, respectively. The vectors $\mathbf{a}_1$ and $\mathbf{a}_2$ are the current directions of the 2 fibers constituents.

The only constituents that undergo G&R in this model are the 2 fiber families and this characteristic allows Eq. (37) to be our candidate of choice for this section. The expression describing the growth of these constituents is shown in Appendix J.

The SED of the elastin constituent used here is the one shown in Eq. (38) and the anisotropic SED $\hat{\psi}^f_e$ of the dispersed fibers is (Gasser et al., 2006):

$$
\begin{aligned}
&\psi^f_e = \hat{\psi}^f_e + U^f_e \\
&\hat{\psi}^f_e(\mathbf{C}_e) = \frac{k_1}{2\,k_2}\left[\exp\left\{k_2\left[\kappa \bar{I}_1 + (1-3\kappa)\bar{I}_4 - 1\right]^2\right\} - 1\right] \\
&\bar{I}_1 = \mathrm{tr}\left[\left(I^f_3\right)^{-2/3}\mathbf{C}_e\right] \\
&\bar{I}_4 = \frac{\left(I^f_3\right)^{-2/3}}{\mathbf{C}_{gr} : (\mathbf{a}_0 \otimes \mathbf{a}_0)}\left[\mathbf{C} : (\mathbf{a}_0 \otimes \mathbf{a}_0)\right] \\
&U^f_e = \frac{\Lambda^f}{2}\left[I^f_3 - 1\right]^2, \\
&I^f_3 = \sqrt{|\mathbf{b}_e|}, \\
&\mathbf{C}_{gr} = \mathbf{F}^T_g\,\mathbf{C}_r\,\mathbf{F}_g,
\end{aligned}
\tag{40}
$$

where $\mathbf{a}_0$ is the fiber direction in reference configuration.

The boundary condition of the test model is of the dirichlet type and it is represented by "λ" in Fig. 7. The prescribed displacement is set under 2 distinct conditions in order to analyze the evolution of the fiber stresses':

- **Stage 1:** ($t < T$) At this stage, the model is set with an initial configuration, which is under homeostasis. Then, the tissue is monotonically stretched up to "$\lambda = 1.1$" under a period of 100 simulated

Table 2: Material parameters used for the mixture model. In this example, 2 fibers were implemented and they only differ in orientation (i.e., the variable "φ").

Constituent	Parameters	Value
Elastin Eq. (38)	ρ_0^e [kg/m^3]	241.5
	μ [J/kg]	12.42
	Λ [J/kg]	20 μ
Dispersed fibers Eq. (40)	ρ_0^f [kg/m^3]	404.25
	k_1 [J/kg]	352.74
	k_2 [−]	4.45
	κ [−]	0.046
	Λ [−]	20 k_1
	φ [degrees]	$\pm 10^o$
	T [days]	100
	α [−] (Appendix J)	10^{-9}

days, a time frame which is equivalent to the prescribed mass turnover "T" of the dispersed fibers (see Tab. 2). This time setting allows the fiber constituents to undergo growth and remodel, while being stretched. A purely elastic case is also run at this stage, so as to analyze the effects of G&R on the stresses of the fibers.

- **Stage 2:** $(T < t < 8T)$

  After reaching a prescribed stretch of "$\lambda = 1.1$", the boundary condition is kept constant and the simulation is run up to 800 simulated days (i.e., "$t = 8T$"). Since the model is fixed and the simulated period is much larger than the mass turnover "T" (see Tab. 2), it is expected that the fibers' stresses will be driven towards its homeostatic state.

The parameters used in each constituent of the material is shown in Tab. 2 and the simulation was run using the Newton-Raphson algorithm represented in Eq. (37). Fig. 8 shows the evolution of one of the fibers' stresses during the first 100 simulated days. The model starts at homeostasis and the stress increases as the tissue is continuously stretched.

Also, since the simulated time frame is equivalent to the fibers' mass turnover "T", the G&R algorithm is able to significantly affect the stress configuration of the fibers. This is seen more clearly, by analyzing the stress evolution alongside a purely elastic case (shown in the same figure) and it is evident that the current framework enables the fiber constituents to return to their homeostatic state.

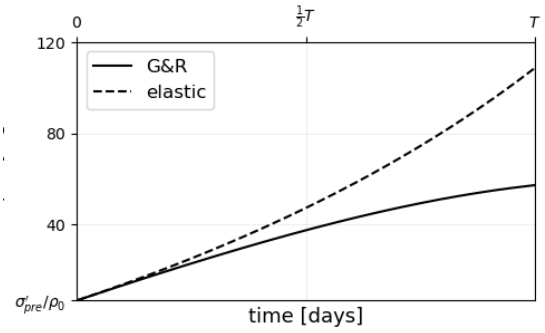

Figure 8: Evolution of stress of the fiber pointing at the direction "$\mathbf{a}_1$", while being continuously pulled. The variable shown in the figure is "$\boldsymbol{\sigma}' : (\mathbf{a}_1 \otimes \mathbf{a}_1)/\rho_0$". The solid line shows the stress configuration, if Eq. (37) is implemented. The dashed lines presented the same model, while assuming the constituents to behave elastically.

The tendency towards returning to a homeostatic stress configuration becomes more evident by analyzing the results obtained in "**Stage 2**" and they are presented in Fig. 9. Since the tissue is fixed between 100 and 800 simulated days, the fibers are free to undergo G&R until its stress configuration reaches homeostasis.

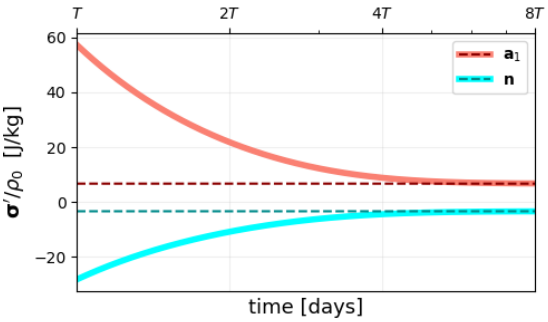

Figure 9: Solid lines: Evolution of the stress components "$\boldsymbol{\sigma}' : (\mathbf{a}_1 \otimes \mathbf{a}_1)$" (red) and "$\boldsymbol{\sigma}' : (\mathbf{n} \otimes \mathbf{n})$" (blue). Dashed lines: homeostatic targets "$\boldsymbol{\sigma}'_{pre} : (\mathbf{a}_1 \otimes \mathbf{a}_1)$" (red) and "$\boldsymbol{\sigma}'_{pre} : (\mathbf{n} \otimes \mathbf{n})$" (blue).

5. Discussion and concluding remarks

In the current paper, for the first time, we provide explicit and ready-to-use expressions describing remodeling of 3D isotropic and anisotropic materials using the H-CMT. Our approach uses similar expressions as in *kinematic hardening* models in standard plasticity. These expressions were obtained by transforming the rate-like equation of the H-CMT [Eq. (13)] into incremental-type equation [Eq. (20)], where an equivalent backstress tensor arises naturally.

Standard numerical strategies of classical plasticity, such as the exponential time-integration scheme, were

implemented here to expand the works of Cyron et al. (2016) to 3D materials. As several modeled biological tissues are assumed to be incompressible, this technique could be used in Eq. (20) as well.

We were able to demonstrate the capabilities of our algorithms with several test cases (Sec. 4). In all examples, the simulations provided physically consistent results. With the simplest case [Sec. 4.1 (no mass variation)], we showed that the model clearly evolves from a stress-free state towards homeostasis (determined by $\boldsymbol{\sigma}'_{pre}$) with Eq. (31).

The model was also validated against experimental data in cell-seeded collagen (Eichinger et al., 2020). Moreover, we showed that the algorithm is sensitive to rates of mass deposition and degradation. Moreover, in Fig. 5, we showed that the larger the mass deposition, the faster the internal tension reaches homeostasis ($\boldsymbol{\sigma}'_{pre}$).

We also explored interactions among anisotropic constituents, which are governed by Eqs. (31) or (35). These interactions are accounted for with a "coupling sub-matrix" [presented in Eqs. (36) and (37)]. The results shown in Fig. 8 and Fig. 9 show that the proposed coupling also simulates G&R of anisotropic constituents within a mixture.

Lastly, it should be noted that the the proposed coupling is a direct consequence of the chosen assumptions related to the growth deformation gradient $\mathbf{F}_g$. As a major application of our models are related to vascular grafts, veins and arteries, it was reasonable to restrict growth to a single direction [Eq. (3)] (Braeu et al., 2017). This simplification permitted to only elaborate a scalar residual related to the constituent's density [Eq. (33)]. In applications where a more general growth tensor would be needed, a tensor residual should be developed instead. Its implementation would go beyond the scope of this work and but an algorithm of anisotropic growth was recently proposed (Lamm et al., 2022).

6. Acknowledgments

This research was financially supported by the European Union's Horizon 2020 research and innovation programme (Grant Agreement 101017523). We would also like to acknowledge prof. Koichi Hashigushi for making her return mapping algorithm publicly available. Her code was essential for the authors to relate remodeling with plasticity. We would also like to thank Eichinger & Cyron for sharing their raw experimental data and for authorizing us to publish them here.

Appendix A. Assumptions of Eq. (20)

Here, we explain the implications of the assumed features in Sec. 2.3. The first bullet-point is related to transforming the problem from its original rate-like form [Eq. (13)] to its incremental variant [Eq. (16)].

That time discretization is widely used in standard finite plasticity, even thought the original problem is stated with rate constitutive laws and evolution equations. However, the expressions are usually solved at an established load or time increment. This requires the rate-like expressions to be integrated over a time interval (t_n and t_{n+1}) and they are reformulated with their equivalent expressions in incremental form.

This is a common strategy to update the stresses and inelastic terms at t_{n+1}. The incremental setting is typically formulated with the backward (implicit) Euler scheme (Bonet and Wood, 1997; Hashiguchi and Yamakawa, 2012; de Souza Neto et al., 2011; Simo, 1992), as it is unconditionally stable. For this reason, the authors decided to discretize Eq. (13) with that same scheme and the following expression is obtained:

$$\boldsymbol{\sigma}\left(t_{n+1}\right) = \left(\frac{\triangle\, \rho_{0+}}{\triangle\, \rho_{0+} + \rho_0}\right)_{k+1} \boldsymbol{\sigma}_{pre} + \left(\frac{\rho_0}{\triangle\, \rho_{0+} + \rho_0}\right)_{k+1} \boldsymbol{\sigma}\left(t_n\right). \tag{A.1}$$

The next bullet-point addresses the assumption of volume-preserving remodeling. Incompressibility is a feature that is often imposed in modeled biological tissues with isotropic constituents (Gasser et al., 2006) and the evolution of an incompressible remodeling is also used by Cyron et al. (2016) and Braeu et al. (2017). Hence, it is assumed that $|\mathbf{F}_r| = const.$ for all time increments. Also, since $\mathbf{F}$ and $\mathbf{F}_g$ are constant quantities between t_n and t_{n+1}, so are their jacobians ($|\mathbf{F}|$ & $|\mathbf{F}_g|$). As $|\mathbf{F}_r|$ is now fixed, it is also implied that

$$|\mathbf{F}_e|_{n+1} = |\mathbf{F}_e|_n. \tag{A.2}$$

The next assumption is that the SED of the isotropic material is composed of a volumetric and distortional SED, such that

$$\psi_e \equiv \hat{\psi}_e(\mathbf{C}_e) + U_e(|\mathbf{F}_e|), \tag{A.3}$$

being $\hat{\psi}_e$ the distortional SED and U_e, the volumetric component. Thanks to Eqs. (A.2, A.3), it is implied that the volumetric contributions of the stresses do not alter between t_n and t_{n+1}.

The last bullet-point is then introduced: we postulate that the volumetric component of the preferred stress $\boldsymbol{\sigma}_{pre}$ and of the current stress are equal. It then necessarily follows from Eq. (A.1) that only the isochoric components of the stresses contribute to the evolution

of remodeling. That equation is now pressure insensitive and it follows that

$$\boldsymbol{\sigma}'(t_{n+1}) = \left(\frac{\triangle\,\rho_{0+}}{\triangle\,\rho_{0+}+\rho_0}\right)_{k+1}\boldsymbol{\sigma}'_{pre} + \left(\frac{\rho_0}{\triangle\,\rho_{0+}+\rho_0}\right)_{k+1}\boldsymbol{\sigma}'(t_n)\,. \tag{A.4}$$

Eq. (A.4) is then used to derive the equivalent yield function in Sec. 2.3.

Appendix B. Elements of $\mathbf{J}_{PG}$ [Eq. (31)]

The elements of the jacobian matrix $\mathbf{J}_{PG}$ shown in Eq. (31) are shown below:

$$\begin{aligned}
&\left[\frac{\partial \mathbf{R}_{\mathbf{C}_r}}{\partial \mathbf{C}_r}\right]_{ijkl} = \mathcal{I}_{ijkl}... \\
&\quad - \frac{\partial \mathbf{Q}_{im}}{\partial \mathbf{C}_{r_{kl}}}\mathbf{C}_{r_{mn}}\mathbf{Q}^T_{mj} - \mathbf{Q}_{io}\mathbf{C}_{r_{op}}\frac{\partial \mathbf{Q}^T_{pj}}{\partial \mathbf{C}_{r_{kl}}}, \\
&\frac{\partial \mathbf{R}_{\mathbf{C}_r}}{\partial \triangle\lambda} = -\frac{\partial \mathbf{Q}}{\partial \triangle\lambda}\mathbf{C}_r\mathbf{Q}^T - \mathbf{Q}\mathbf{C}_r\frac{\partial \mathbf{Q}^T}{\partial \triangle\lambda}, \\
&\left[\frac{\partial R_f}{\partial \mathbf{C}_r}\right]_{ij} = \left[\frac{\partial f}{\partial \hat{\hat{\mathbf{M}}}}\right]_{mn}\left[\frac{\partial \hat{\hat{\mathbf{M}}}}{\partial \mathbf{C}_r}\right]_{mnij}, \\
&\frac{\partial R_f}{\partial \triangle\lambda} = 0,
\end{aligned} \tag{B.1}$$

$$\begin{aligned}
&\mathcal{I}_{ijkl} = \frac{1}{2}\left(\delta_{ik}\delta_{jl} + \delta_{il}\delta_{jk}\right), \\
&\frac{\partial f}{\partial \hat{\hat{\mathbf{M}}}} = \hat{\hat{\mathbf{M}}}'^T, \\
&\left[\frac{\partial \mathbf{Q}}{\partial \mathbf{C}_r}\right]_{ijkl} = \left[\frac{\partial \mathbf{Q}}{\partial \mathbf{Z}}\right]_{ijmn}\left[\frac{\partial \mathbf{Z}}{\partial \mathbf{C}_r}\right]_{mnkl}, \\
&\left[\frac{\partial \mathbf{Q}^T}{\partial \mathbf{C}_r}\right]_{ijkl} = \delta_{in}\delta_{jm}\left[\frac{\partial \mathbf{Q}}{\partial \mathbf{C}_r}\right]_{mnkl}, \\
&\left[\frac{\partial \mathbf{Q}}{\partial \triangle\lambda}\right]_{ij} = \left[\frac{\partial \mathbf{Q}}{\partial \mathbf{Z}}\right]_{ijmn}\left[\frac{\partial \mathbf{Z}}{\partial \triangle\lambda}\right]_{mn}
\end{aligned} \tag{B.2}$$

The term $\frac{\partial \mathbf{Q}}{\partial \mathbf{Z}}$ [present in Eqs. (B.2, C.1, D.1)] were explicitly derived by Hashiguchi and Yamakawa (2012). As for $\frac{\partial \mathbf{Z}}{\partial \mathbf{C}_r}$ & $\frac{\partial \mathbf{Z}}{\partial \triangle\lambda}$, they are presented in Appendix F.

Appendix C. Elements of $\mathbf{J}_{GR\rightarrow PG}$ [Eq. (36)]

The remaining elements of the sub-matrix $\mathbf{J}_{GR\rightarrow PG}$ [Eq. (36) and displayed in Fig. 2 (a)] that must be derived are the tensors $\frac{\partial \mathbf{R}^a_{\mathbf{C}_r}}{\partial \rho^b_0}$ and $\frac{\partial R^a_f}{\partial \rho^b_0}$:

$$\begin{aligned}
&\frac{\partial \mathbf{R}^a_{\mathbf{C}_r}}{\partial \rho^b_0} = -\frac{\partial \mathbf{Q}^a}{\partial \rho^b_0}\mathbf{C}_r\mathbf{Q}^T - \mathbf{Q}\mathbf{C}_r\frac{\partial \mathbf{Q}^{aT}}{\partial \rho^b_0}, \\
&\frac{\partial R^a_f}{\partial \rho^b_0} = \left[\frac{\partial f^a}{\partial \hat{\hat{\mathbf{M}}}^a}\right] : \left[\frac{\partial \hat{\hat{\mathbf{M}}}^a}{\partial \rho^b_0}\right], \\
&\left[\frac{\partial \mathbf{Q}^a}{\partial \rho^b_0}\right]_{ij} = \left[\frac{\partial \mathbf{Q}^a}{\partial \mathbf{Z}^a}\right]_{ijmn}\left[\frac{\partial \mathbf{Z}^a}{\partial \rho^b_0}\right]_{mn},
\end{aligned} \tag{C.1}$$

Appendix D. Elements of $\mathbf{J}_{GR}$ [Eq. (35)]

The tensors $\frac{\partial \mathbf{R}_{\mathbf{C}_r}}{\partial \mathbf{C}_r}$, $\frac{\partial \mathbf{R}_{\mathbf{C}_r}}{\partial \triangle\lambda}$, $\frac{\partial R_f}{\partial \mathbf{C}_r}$ and $\frac{\partial R_f}{\partial \triangle\lambda}$ of Eq. (35) are identical to the expressions shown in Eq. (B.1). All other tensors that must be defined for the "*growth & remodeling*" case are displayed below:

$$\begin{aligned}
&\frac{\partial \mathbf{R}_{\mathbf{C}_r}}{\partial \rho_0} = -\frac{\partial \mathbf{Q}}{\partial \rho_0}\mathbf{C}_r\mathbf{Q}^T - \mathbf{Q}\mathbf{C}_r\frac{\partial \mathbf{Q}^T}{\partial \rho_0}, \\
&\frac{\partial R_f}{\partial \rho_0} = \left[\frac{\partial f}{\partial \hat{\hat{\mathbf{M}}}}\right] : \left[\frac{\partial \hat{\hat{\mathbf{M}}}}{\partial \rho_0}\right], \\
&\frac{\partial R_{\rho_0}}{\partial \mathbf{C}_r} = -\triangle t\frac{\partial \dot{\rho}_0}{\partial \mathbf{C}_r}, \\
&\frac{\partial R_{\rho_0}}{\partial \triangle\lambda} = 0, \\
&\frac{\partial R_{\rho_0}}{\partial \rho_0} = 1 - \triangle t\frac{\partial \dot{\rho}_0}{\partial \rho_0}, \\
&\left[\frac{\partial \mathbf{Q}}{\partial \rho_0}\right]_{ij} = \left[\frac{\partial \mathbf{Q}}{\partial \mathbf{Z}}\right]_{ijmn}\left[\frac{\partial \mathbf{Z}}{\partial \rho_0}\right]_{mn}.
\end{aligned} \tag{D.1}$$

Appendix E. Elements of $\mathbf{J}_{GR\,b\rightarrow GR\,a}$ [Eq. (37)]

The tensors $\frac{\partial \mathbf{R}^a_{\mathbf{C}_r}}{\partial \rho^b_0}$ and $\frac{\partial R^a_f}{\partial \rho^b_0}$ shown in Eq. (37) can be implemented directly from Eq. (C.1). The remaining derivative that should be defined is

$$\frac{\partial R^a_{\rho_0}}{\partial \rho^b_0} = -\triangle t\frac{\partial \dot{\rho}^a_0}{\partial \rho^b_0}, \tag{E.1}$$

Appendix F. Derivatives of the tensor Z

- **Derivatives of Z:**

$$\begin{aligned}
&\frac{\partial \mathbf{Z}}{\partial \mathbf{C}_r} = \sqrt{2}\triangle\lambda\frac{1}{D}\left\{\frac{\partial \hat{\hat{\mathbf{M}}}'}{\partial \mathbf{C}_r} - \frac{1}{2}\frac{1}{D^2}\hat{\hat{\mathbf{M}}}' \otimes \frac{\partial D^2}{\partial \mathbf{C}_r}\right\}, \\
&\frac{\partial \mathbf{Z}}{\partial \triangle\lambda} = \sqrt{2}\frac{\hat{\hat{\mathbf{M}}}'}{D}, \\
&\frac{\partial \mathbf{Z}}{\partial \rho_0} = \sqrt{2}\triangle\lambda\frac{1}{D}\left\{\frac{\partial \hat{\hat{\mathbf{M}}}'}{\partial \rho_0} - \frac{1}{2}\frac{1}{D^2}\hat{\hat{\mathbf{M}}}'\frac{\partial D^2}{\partial \rho_0}\right\}, \\
&D = \sqrt{\left[\mathbf{C}_r^{-1}\hat{\hat{\mathbf{M}}}'\mathbf{C}_r\right] : \hat{\hat{\mathbf{M}}}' + \hat{\hat{\mathbf{M}}}' : \hat{\hat{\mathbf{M}}}'^T}.
\end{aligned} \tag{F.1}$$

- $\partial D^2/\partial \mathbf{C}_r$**:**

$$\begin{aligned}
&\left[\frac{\partial D^2}{\partial \mathbf{C}_r}\right]_{ij} = \mathbf{T}_1 + \mathbf{T}_2 + \mathbf{T}_3,\\
&[\mathbf{T}_1]_{kl} = \frac{\partial\left[\mathbf{C}_r^{-1}\hat{\tilde{\mathbf{M}}}'\mathbf{C}_r\right]_{mn}}{\partial \mathbf{C}_{r_{kl}}}\hat{\tilde{\mathbf{M}}}'_{mn},\\
&\frac{\partial\left[\mathbf{C}_r^{-1}\hat{\tilde{\mathbf{M}}}'\mathbf{C}_r\right]_{ij}}{\partial \mathbf{C}_{r_{kl}}} = \frac{\partial \mathbf{C}^{-1}_{r_{im}}}{\partial \mathbf{C}_{r_{kl}}}\hat{\tilde{\mathbf{M}}}'_{mn}\mathbf{C}_{r_{nj}} + ...\\
&\quad \mathbf{C}^{-1}_{r_{im}}\frac{\partial \hat{\tilde{\mathbf{M}}}'_{mn}}{\partial \mathbf{C}_{r_{kl}}}\mathbf{C}_{r_{nj}} + \mathbf{C}^{-1}_{r_{im}}\hat{\tilde{\mathbf{M}}}'_{mn}\mathcal{I}_{njkl},\\
&[\mathbf{T}_2]_{kl} = \left[\mathbf{C}_r^{-1}\hat{\tilde{\mathbf{M}}}'\mathbf{C}_r\right]_{mn}\frac{\partial \hat{\tilde{\mathbf{M}}}'_{mn}}{\partial \mathbf{C}_{r_{kl}}},\\
&[\mathbf{T}_3]_{kl} = 2\frac{\partial \hat{\tilde{\mathbf{M}}}'_{mn}}{\partial \mathbf{C}_{r_{kl}}}\hat{\tilde{\mathbf{M}}}'^{T}_{mn}
\end{aligned} \tag{F.2}$$

- $\partial D^2/\partial \rho_0$**:**

$$\begin{aligned}
&\frac{\partial D^2}{\partial \rho_0} = U_1 + U_2 + U_3,\\
&U_1 = \frac{\partial\left[\mathbf{C}_r^{-1}\hat{\tilde{\mathbf{M}}}'\mathbf{C}_r\right]}{\partial \rho_0} : \hat{\tilde{\mathbf{M}}}',\\
&\frac{\partial\left[\mathbf{C}_r^{-1}\hat{\tilde{\mathbf{M}}}'\mathbf{C}_r\right]_{ij}}{\partial \rho_0} = \mathbf{C}^{-1}_{r_{im}}\frac{\partial \hat{\tilde{\mathbf{M}}}'_{mn}}{\partial \rho_0}\mathbf{C}_{r_{nj}},\\
&U_2 = \left[\mathbf{C}_r^{-1}\hat{\tilde{\mathbf{M}}}'\mathbf{C}_r\right] : \frac{\partial \hat{\tilde{\mathbf{M}}}'}{\partial \rho_0},\\
&U_3 = 2\frac{\partial \hat{\tilde{\mathbf{M}}}'}{\partial \rho_0} : \hat{\tilde{\mathbf{M}}}'^{T}
\end{aligned} \tag{F.3}$$

- **Derivatives of** $\hat{\tilde{\mathbf{M}}}'$**:**

$$\begin{aligned}
&\frac{\partial \hat{\tilde{\mathbf{M}}}'_{ij}}{\partial \mathbf{C}_{r_{kl}}} = \mathcal{D}_{ijmn}\frac{\partial \hat{\tilde{\mathbf{M}}}_{mn}}{\partial \mathbf{C}_{r_{kl}}},\\
&\frac{\partial \hat{\tilde{\mathbf{M}}}'_{ij}}{\partial \rho_0} = \mathcal{D}_{ijmn}\frac{\partial \hat{\tilde{\mathbf{M}}}_{mn}}{\partial \rho_0},\\
&\mathcal{D}_{ijkl} = \delta_{ik}\delta_{jl} - \frac{1}{3}\delta_{ij}\delta_{kl}.
\end{aligned} \tag{F.4}$$

Appendix G. Derivatives of the relative stress-like tensors

The residuals shown in Appendix B, Appendix C, Appendix D, Appendix E and the exponential terms in Appendix F are directly or indirectly dependent on the tensors $\frac{\partial \hat{\tilde{\mathbf{M}}}}{\partial \mathbf{C}_r}$, $\frac{\partial \hat{\tilde{\mathbf{M}}}}{\partial \rho_0}$ and $\frac{\partial \hat{\tilde{\mathbf{M}}}^a}{\partial \rho_0^b}$.

The manner by which these terms are computed depend on the algorithm at hand. They are shown next for each case and labeled with the subscripts "*PG*" or "*GR*" to indicate a "*Prescribed Growth*" or "*Growth & Remodeling*", respectively.

- $\mathbf{J}_{PG}$ **[Eq.** (31)**]:**

The remaining tensor that must be defined for the *Prescribed growth* case in Eq. (B.1) is $\frac{\partial \hat{\tilde{\mathbf{M}}}}{\partial \mathbf{C}_r}$. With the help of Eq. (24) and labeling the tensor with the subscript "*PG*", we obtain

$$\left[\left.\frac{\partial \hat{\tilde{\mathbf{M}}}}{\partial \mathbf{C}_r}\right|_{PG}\right]_{ijkl} = \left[\left(\mathbf{F}\mathbf{F}_g^{-1}\right)^T\right]_{im}\left[\left.\frac{\partial \hat{\boldsymbol{\tau}}}{\partial \mathbf{C}_r}\right|_{PG}\right]_{mnkl}\left[\left(\mathbf{F}\mathbf{F}_g^{-1}\right)^{-T}\right]_{nj}. \tag{G.1}$$

The tensor $\left.\frac{\partial \hat{\boldsymbol{\tau}}}{\partial \mathbf{C}_r}\right|_{PG}$ in Eq. (G.1) can be derived from Eq. (19). For the cases, where the growth is prescribed, the remodeling tensor $\mathbf{C}_r$ has no effect on the backstress. Hence, from $\frac{\partial \boldsymbol{\tau}_r}{\partial \mathbf{C}_r}$ is null in Eq. (19) and we finally obtain

$$\left.\frac{\partial \hat{\boldsymbol{\tau}}}{\partial \mathbf{C}_r}\right|_{PG} = \frac{\partial \boldsymbol{\tau}}{\partial \mathbf{C}_r}. \tag{G.2}$$

- $\mathbf{J}_{GR\rightharpoonup PG}$ **[Eq.** (36)**]**

The extra variable that must be defined is $\frac{\partial \hat{\tilde{\mathbf{M}}}^a}{\partial \rho_0^b}$ and it is obtained with Eq. (24):

$$\begin{aligned}
&\left[\left.\frac{\partial \hat{\tilde{\mathbf{M}}}^a}{\partial \rho_0^b}\right|_{PG}\right]_{ij} = ...\\
&\quad\left[\frac{\partial \mathbf{F}_g^{-T}}{\partial \rho_0^b}\right]_{im}\left[\mathbf{F}^T\hat{\boldsymbol{\tau}}^a\mathbf{F}^{-T}\right]_{mn}\left[\mathbf{F}_g^T\right]_{nj} + ...\\
&\quad\left[\left(\mathbf{F}\mathbf{F}_g^{-1}\right)^T\right]_{im}\left[\left.\frac{\partial \hat{\boldsymbol{\tau}}^a}{\partial \rho_0^b}\right|_{PG}\right]_{mn}\left[\left(\mathbf{F}\mathbf{F}_g^{-1}\right)^{-T}\right]_{nj} + ...\\
&\quad\left[\mathbf{F}_g^{-T}\right]_{im}\left[\mathbf{F}^T\hat{\boldsymbol{\tau}}^a\mathbf{F}^{-T}\right]_{mn}\left[\frac{\partial \mathbf{F}_g^T}{\partial \rho_0^b}\right]_{nj}
\end{aligned} \tag{G.3}$$

It is worth reminding the reader that the growth deformation gradients of all constituents are identical in the present work (*i.e.*, $\mathbf{F}_g^a = \mathbf{F}_g$). Due to this and for clarity, the superscript "a" is dropped from $\mathbf{F}_g$ in Eq. (G.3).

The derivative $\frac{\partial \mathbf{F}_g}{\partial \rho_0^b}$ is computed with the help of Eq. (3):

$$\frac{\partial \mathbf{F}_g}{\partial \rho_0^b} = \left[\frac{1}{\rho_{0\,\mathrm{init}}}\right]\mathbf{N}^\perp \otimes \mathbf{N}^\perp. \tag{G.4}$$

Here, the density of "constituent b" *does* affect the backstress of "constituent a" and $\left.\frac{\partial \hat{\boldsymbol{\tau}}^a}{\partial \rho_0^b}\right|_{PG}$ is obtained via Eq. (19):

$$\left.\frac{\partial \hat{\boldsymbol{\tau}}^a}{\partial \rho_0^b}\right|_{PG} = \frac{\partial \boldsymbol{\tau}^a}{\partial \rho_0^b} - \left.\frac{\partial \boldsymbol{\tau}^a_r}{\partial \rho_0^b}\right|_{PG} \tag{G.5}$$

- $\mathbf{J}_{GR}$ [Eq. (35)]

  For the *growth & remodeling* case, the derivatives of the Eshelby-like stress tensors $\frac{\partial \hat{\tilde{\mathbf{M}}}}{\partial \mathbf{C}_r}$ and $\frac{\partial \hat{\tilde{\mathbf{M}}}}{\partial \rho_0}$ are required. They can be computed with the help of Eq. (24):

$$\begin{aligned}
\left[\frac{\partial \hat{\tilde{\mathbf{M}}}}{\partial \mathbf{C}_r}\bigg|_{GR}\right]_{ijkl} &= \left[\left(\mathbf{F}\mathbf{F}_g^{-1}\right)^T\right]_{im}\left[\frac{\partial \hat{\boldsymbol{\tau}}}{\partial \mathbf{C}_r}\bigg|_{GR}\right]_{mnkl}\left[\left(\mathbf{F}\mathbf{F}_g^{-1}\right)^{-T}\right]_{nj},\\
\left[\frac{\partial \hat{\tilde{\mathbf{M}}}}{\partial \rho_0}\right]_{ij} &= \left[\frac{\partial \mathbf{F}_g^{-T}}{\partial \rho_0}\right]_{im}\left[\mathbf{F}^T\hat{\boldsymbol{\tau}}\mathbf{F}^{-T}\right]_{mn}\left[\mathbf{F}_g^T\right]_{nj} + ...\\
&\quad \left[\left(\mathbf{F}\mathbf{F}_g^{-1}\right)^T\right]_{im}\left[\frac{\partial \hat{\boldsymbol{\tau}}}{\partial \rho_0}\right]_{mn}\left[\left(\mathbf{F}\mathbf{F}_g^{-1}\right)^{-T}\right]_{nj} + ...\\
&\quad \left[\mathbf{F}_g^{-T}\right]_{im}\left[\mathbf{F}^T\hat{\boldsymbol{\tau}}\mathbf{F}^{-T}\right]_{mn}\left[\frac{\partial \mathbf{F}_g^T}{\partial \rho_0}\right]_{nj}.
\end{aligned} \tag{G.6}$$

  The terms related to $\frac{\partial \mathbf{F}_g}{\partial \rho_0}$ in Eq. (G.6) are obtained directly from Eq. (3):

$$\frac{\partial \mathbf{F}_g}{\partial \rho_0} = \left[\frac{1}{\rho_{0\,\mathrm{init}}}\right]\mathbf{N}^{\perp}\otimes\mathbf{N}^{\perp} \tag{G.7}$$

  It was mentioned in Appendix B that the backstress is independent from remodeling in the "*prescribed growth*" case. This does not hold for a "*growth & remodeling*" material, as the updated density is not known beforehand. Since the backstress is now indirectly dependent on remodeling and the density, it follows from Eq. (19) that:

$$\begin{aligned}
\frac{\partial \hat{\boldsymbol{\tau}}}{\partial \mathbf{C}_r}\bigg|_{GR} &= \frac{\partial \boldsymbol{\tau}}{\partial \mathbf{C}_r} - \frac{\partial \boldsymbol{\tau}_r}{\partial \mathbf{C}_r},\\
\frac{\partial \hat{\boldsymbol{\tau}}}{\partial \rho_0} &= \frac{\partial \boldsymbol{\tau}}{\partial \rho_0} - \frac{\partial \boldsymbol{\tau}_r}{\partial \rho_0}.
\end{aligned} \tag{G.8}$$

- $\mathbf{J}_{GR\,b\rightarrow GR\,a}$ **[Eq.** (37)**]**

  The tensor $\frac{\partial \hat{\tilde{\mathbf{M}}}^a}{\partial \rho_0^b}$ must be defined here:

$$\begin{aligned}
\left[\frac{\partial \hat{\tilde{\mathbf{M}}}^a}{\partial \rho_0^b}\bigg|_{GR}\right]_{ij} &= ...\\
&\quad \left[\frac{\partial \mathbf{F}_g^{-T}}{\partial \rho_0^b}\right]_{im}\left[\mathbf{F}^T\hat{\boldsymbol{\tau}}^a\mathbf{F}^{-T}\right]_{mn}\left[\mathbf{F}_g^T\right]_{nj} + ...\\
&\quad \left[\left(\mathbf{F}\mathbf{F}_g^{-1}\right)^T\right]_{im}\left[\frac{\partial \hat{\boldsymbol{\tau}}^a}{\partial \rho_0^b}\bigg|_{GR}\right]_{mn}\left[\left(\mathbf{F}\mathbf{F}_g^{-1}\right)^{-T}\right]_{nj} + ...\\
&\quad \left[\mathbf{F}_g^{-T}\right]_{im}\left[\mathbf{F}^T\hat{\boldsymbol{\tau}}^a\mathbf{F}^{-T}\right]_{mn}\left[\frac{\partial \mathbf{F}_g^T}{\partial \rho_0^b}\right]_{nj}.
\end{aligned} \tag{G.9}$$

  In this case, the backstress is also affected by the updated densities of other constituents within the mixture. Hence,

$$\frac{\partial \hat{\boldsymbol{\tau}}^a}{\partial \rho_0^b}\bigg|_{GR} = \frac{\partial \boldsymbol{\tau}^a}{\partial \rho_0^b} - \frac{\partial \boldsymbol{\tau}_r^a}{\partial \rho_0^b}\bigg|_{GR}. \tag{G.10}$$

Appendix H. Derivatives of the backstresses

This appendix shows the derivatives of the backstresses shown in Appendix G:

- **Eq.** (G.5)

$$\frac{\partial \boldsymbol{\tau}_r^a}{\partial \rho_0^b}\bigg|_{PG} = \left[\frac{\rho_0^a}{\rho_0^a + \triangle\rho_{0+}^a}\right]\frac{\partial \boldsymbol{\tau}_n^a}{\partial \rho_0^b} \tag{H.1}$$

- **Eq.** (G.8)

$$\begin{aligned}
&\left[\frac{\partial \boldsymbol{\tau}_r}{\partial \mathbf{C}_r}\right]_{ijkl} = ...\\
&\quad \left[\frac{\partial\left(\rho_0 + \triangle\rho_{0+}\right)^{-1}}{\partial \mathbf{C}_r}\right]_{kl}\left[\triangle\rho_{0+}\boldsymbol{\tau}_{pre} + \rho_0\boldsymbol{\tau}_n\right]_{ij} + ...\\
&\quad \left[\rho_0 + \triangle\rho_{0+}\right]^{-1}\left[\frac{\partial \triangle\rho_{0+}}{\partial \mathbf{C}_r}\right]_{kl}\left[\boldsymbol{\tau}_{pre}\right]_{ij}\\
&\frac{\partial \boldsymbol{\tau}_r}{\partial \rho_0} = ...\\
&\quad \left[\frac{\partial\left(\rho_0 + \triangle\rho_{0+}\right)^{-1}}{\partial \rho_0}\right]\left[\triangle\rho_{0+}\boldsymbol{\tau}_{pre} + \rho_0\boldsymbol{\tau}_n\right] + ...\\
&\quad \left[\rho_0 + \triangle\rho_{0+}\right]^{-1}\left[\frac{\partial \triangle\rho_{0+}}{\partial \rho_0}\boldsymbol{\tau}_{pre} + \boldsymbol{\tau}_n + \rho_0\frac{\partial \boldsymbol{\tau}_n}{\partial \rho_0}\right]
\end{aligned} \tag{H.2}$$

  where

$$\begin{aligned}
\frac{\partial\left(\rho_0 + \triangle\rho_{0+}\right)^{-1}}{\partial \mathbf{C}_r} &= -\left(\rho_0 + \triangle\rho_{0+}\right)^{-2}\left(\frac{\partial \triangle\rho_{0+}}{\partial \mathbf{C}_r}\right),\\
\frac{\partial \triangle\rho_{0+}}{\partial \mathbf{C}_r} &= \triangle t\frac{\partial \dot{\rho_0}}{\partial \mathbf{C}_r},\\
\frac{\partial\left(\rho_0 + \triangle\rho_{0+}\right)^{-1}}{\partial \rho_0} &= -\left(\rho_0 + \triangle\rho_{0+}\right)^{-2}\left(1 + \frac{\partial \triangle\rho_{0+}}{\partial \rho_0}\right),\\
\frac{\partial \triangle\rho_{0+}}{\partial \rho_0} &= \triangle t\frac{\partial \dot{\rho_0}}{\partial \rho_0} + \frac{\triangle t}{T}.
\end{aligned} \tag{H.3}$$

- **Eq.** (G.10)

$$\begin{aligned}
&\frac{\partial \boldsymbol{\tau}_r^a}{\partial \rho_0^b}\bigg|_{GR} = ...\\
&\quad \left[\frac{\partial\left(\rho_0^a + \triangle\rho_{0+}^a\right)^{-1}}{\partial \rho_0^b}\right]\left[\triangle\rho_{0+}^a\boldsymbol{\tau}_{pre}^a + \rho_0^a\boldsymbol{\tau}_n^a\right] + ...\\
&\quad \left[\rho_0^a + \triangle\rho_{0+}^a\right]^{-1}\left[\frac{\partial \triangle\rho_{0+}^a}{\partial \rho_0^b}\boldsymbol{\tau}_{pre}^a + \rho_0^a\frac{\partial \boldsymbol{\tau}_n^a}{\partial \rho_0^b}\right],
\end{aligned} \tag{H.4}$$

  where

$$\begin{aligned}
\frac{\partial\left(\rho_0^a + \triangle\rho_{0+}^a\right)^{-1}}{\partial \rho_0^b} &= -\left(\rho_0^a + \triangle\rho_{0+}^a\right)^{-2}\left(\frac{\partial \triangle\rho_{0+}^a}{\partial \rho_0^b}\right)\\
\frac{\partial \triangle\rho_{0+}^a}{\partial \rho_0^b} &= \triangle t\frac{\partial \dot{\rho_0^a}}{\partial \rho_0^b}
\end{aligned} \tag{H.5}$$

Appendix I. Derivatives of the current stresses

The Eqs. (G.2), (G.5), (G.8) and (G.10) also depend on derivatives of the current stress $\boldsymbol{\tau}$. In this work, we demonstrated our results with a Nearly Incompressible Neo-Hookean SED [Eq. (38)], but it is also applicable to other material types as well. As to generalize the current derivation, we assume that the stress is a function of the left Cauchy–Green deformation tensor $\mathbf{b}_e$, and its invariants I_1 and I_3:

$$\begin{aligned} \boldsymbol{\tau} &\equiv \boldsymbol{\tau}\left(\mathbf{b}_e, I_1, I_3\right), \\ I_1 &= \mathbf{b}_e : \mathbf{I}, \\ I_3 &= \sqrt{|\mathbf{b}_e|}. \end{aligned} \tag{I.1}$$

Therefore, the derivatives of the stress w.r.t. $\mathbf{C}_r$ [Eqs. (G.2, G.8)] and "ρ_0" [Eqs. (G.5, G.8, G.10)] can be represented as

$$\begin{aligned} \frac{\partial \boldsymbol{\tau}}{\partial \mathbf{C}_r} &\equiv \frac{\partial \boldsymbol{\tau}}{\partial \mathbf{C}_r}\left(\frac{\partial \mathbf{b}_e}{\partial \mathbf{C}_r}, \frac{\partial I_1}{\partial \mathbf{C}_r}, \frac{\partial I_3}{\partial \mathbf{C}_r}\right), \\ \frac{\partial \boldsymbol{\tau}}{\partial \rho_0} &\equiv \frac{\partial \boldsymbol{\tau}}{\partial \rho_0}\left(\frac{\partial \mathbf{b}_e}{\partial \rho_0}, \frac{\partial I_1}{\partial \rho_0}, \frac{\partial I_3}{\partial \rho_0}\right). \end{aligned} \tag{I.2}$$

By representing the tensor $\mathbf{b}_e$ with the total deformation and the inelastic terms, we obtain:

$$\mathbf{b}_e = \mathbf{F}\mathbf{F}_g^{-1}\mathbf{C}_r^{-1}\mathbf{F}_g^{-T}\mathbf{F}^T. \tag{I.3}$$

With Eq. (I.3), we can compute the derivatives required in Eq. (I.2) and the explicit derivations are presented below:

$$\begin{aligned} \left[\frac{\partial \mathbf{b}_e}{\partial \mathbf{C}_r}\right]_{ijkl} &= \left[\mathbf{F}\mathbf{F}_g^{-1}\right]_{im}\left[\frac{\partial \mathbf{C}_r^{-1}}{\partial \mathbf{C}_r}\right]_{mnkl}\left[\mathbf{F}_g^{-T}\mathbf{F}^T\right]_{nj}, \\ \left[\frac{\partial I_1}{\partial \mathbf{C}_r}\right]_{kl} &= \left[\frac{1}{2}\, I_1\, \mathbf{b}_e^{-1}\right]_{mn}\left[\frac{\partial \mathbf{b}_e}{\partial \mathbf{C}_r}\right]_{mnkl}, \\ \left[\frac{\partial I_3}{\partial \mathbf{C}_r}\right]_{kl} &= \delta_{mn}\left[\frac{\partial \mathbf{b}_e}{\partial \mathbf{C}_r}\right]_{mnkl}, \\ \left[\frac{\partial \mathbf{C}_r^{-1}}{\partial \mathbf{C}_r}\right]_{ijkl} &= -\frac{1}{2}\left\{\left[\mathbf{C}_r^{-1}\right]_{ik}\left[\mathbf{C}_r^{-1}\right]_{lj} + \left[\mathbf{C}_r^{-1}\right]_{jk}\left[\mathbf{C}_r^{-1}\right]_{li}\right\}, \\ \frac{\partial \mathbf{b}_e}{\partial \rho_0} &= \mathbf{F}\left[\frac{\partial \mathbf{F}_g^{-1}}{\partial \rho_0}\right]\mathbf{C}_r^{-1}\mathbf{F}_g^{-T}\mathbf{F}^T + \mathbf{F}\mathbf{F}_g^{-1}\mathbf{C}_r^{-1}\left[\frac{\partial \mathbf{F}_g^{-T}}{\partial \rho_0}\right]\mathbf{F}^T, \\ \frac{\partial I_1}{\partial \rho_0} &= \left[\frac{1}{2}\, I_1\, \mathbf{b}_e^{-1}\right] : \left[\frac{\partial \mathbf{b}_e}{\partial \rho_0}\right], \\ \frac{\partial I_3}{\partial \rho_0} &= \left[\frac{\partial \mathbf{b}_e}{\partial \rho_0}\right] : \mathbf{I}. \end{aligned} \tag{I.4}$$

Finally, the tensors $\frac{\partial \boldsymbol{\tau}}{\partial \mathbf{C}_r}$ and $\frac{\partial \boldsymbol{\tau}}{\partial \rho_0}$ can be finally obtained.

Appendix J. Stress-induced density rules

The density rate expression used in Sec. 4.2 is an adaptation of the rule proposed by Drews et al. (2020). They created such rules for unidimensional fibers only and they are dependent on their scalar stresses and pseudo-invariants I_4. As we work with isotropic materials, the aforementioned inputs were modified to the invariants J_2 and I_1:

$$\begin{aligned} \dot{\rho}_0 &= \dot{\rho}_{0+}^D + \dot{\rho}_{0-}^D, \\ \dot{\rho}_{0+}^D &= m_h\left[1 - \exp(-t)\right]\left[1 + K_\sigma\left(\frac{J_2}{J_2^h} - 1\right)\right], \\ \dot{\rho}_{0-}^D &= k_h \rho_0^D\left[\left(1 + \frac{I_1}{I_1^h}\right)^2\right]. \end{aligned} \tag{J.1}$$

being

$$\begin{aligned} J_2^h &= \frac{1}{2}\boldsymbol{\tau}'_{pre} : \boldsymbol{\tau}'_{pre}, \\ I_1^h &= \mathbf{F}_h : \mathbf{I}. \end{aligned} \tag{J.2}$$

The numerical experiment in Sec. 4.3 required a density rate expression for the dispersed fibers and it is shown below:

$$\begin{aligned} \dot{\rho}_0 &= \alpha\, \rho_0\, f_g \\ f_g &= \frac{1}{2}(\boldsymbol{\tau}' - \boldsymbol{\tau}'_{pre}) : (\boldsymbol{\tau}' - \boldsymbol{\tau}'_{pre}). \end{aligned} \tag{J.3}$$

References

Blum, K.M., Zbinden, J.C., Ramachandra, A.B., Lindsey, S.E., Szafron, J.M., Reinhardt, J.W., Heitkemper, M., Best, C.A., Mirhaidari, G.J., Chang, Y.C., et al., 2022. Tissue engineered vascular grafts transform into autologous neovessels capable of native function and growth. Communications medicine 2, 1–21.

Bonet, J., Wood, R.D., 1997. Nonlinear continuum mechanics for finite element analysis. Cambridge university press.

Braeu, F., Seitz, A., Aydin, R., Cyron, C., 2017. Homogenized constrained mixture models for anisotropic volumetric growth and remodeling. Biomechanics and modeling in mechanobiology 16, 889–906.

Cardamone, L., Valentin, A., Eberth, J., Humphrey, J., 2010. Modelling carotid artery adaptations to dynamic alterations in pressure and flow over the cardiac cycle. Mathematical medicine and biology: a journal of the IMA 27, 343–371.

Cyron, C., Aydin, R., 2017. Mechanobiological free energy: a variational approach to tensional homeostasis in tissue equivalents. ZAMM-Journal of Applied Mathematics and Mechanics/Zeitschrift für Angewandte Mathematik und Mechanik 97, 1011–1019.

Cyron, C., Aydin, R., Humphrey, J., 2016. A homogenized constrained mixture (and mechanical analog) model for growth and remodeling of soft tissue. Biomechanics and modeling in mechanobiology 15, 1389–1403.

Cyron, C., Humphrey, J., 2017. Growth and remodeling of load-bearing biological soft tissues. Meccanica 52, 645–664.

Drews, J.D., Pepper, V.K., Best, C.A., Szafron, J.M., Cheatham, J.P., Yates, A.R., Hor, K.N., Zbinden, J.C., Chang, Y.C., Mirhaidari, G.J., et al., 2020. Spontaneous reversal of stenosis in tissue-engineered vascular grafts. Science translational medicine 12, eaax6919.

Eichinger, J.F., Paukner, D., Szafron, J.M., Aydin, R.C., Humphrey, J.D., Cyron, C.J., 2020. Computer-controlled biaxial bioreactor for investigating cell-mediated homeostasis in tissue equivalents. Journal of biomechanical engineering 142, 071011.

Fung, Y.C.B., 1973. Biorheology of soft tissues. Biorheology 10, 139–155.

Gasser, T.C., Ogden, R.W., Holzapfel, G.A., 2006. Hyperelastic modelling of arterial layers with distributed collagen fibre orientations. Journal of the royal society interface 3, 15–35.

Ghavamian, A., Mousavi, S.J., Avril, S., 2020. Computational study of growth and remodeling in ascending thoracic aortic aneurysms considering variations of smooth muscle cell basal tone. Frontiers in Bioengineering and Biotechnology 8, 587376.

Grillo, A., Stefano, S.D., Ramírez-Torres, A., Loverre, M., 2019. A study of growth and remodeling in isotropic tissues, based on the anand-aslan-chester theory of strain-gradient plasticity. GAMM-Mitteilungen 42, e201900015.

Gurtin, M.E., Fried, E., Anand, L., 2010. The mechanics and thermodynamics of continua. Cambridge University Press.

Hashiguchi, K., 2019. Multiplicative hyperelastic-based plasticity for finite elastoplastic deformation/sliding: A comprehensive review. Archives of Computational Methods in Engineering 26, 597–637.

Hashiguchi, K., Yamakawa, Y., 2012. Introduction to finite strain theory for continuum elasto-plasticity. John Wiley & Sons.

Holzapfel, G.A., Gasser, T.C., Ogden, R.W., 2000. A new constitutive framework for arterial wall mechanics and a comparative study of material models. Journal of elasticity and the physical science of solids 61, 1–48.

Horvat, N., Virag, L., Holzapfel, G.A., Karšaj, I., 2021. Implementation of collagen fiber dispersion in a growth and remodeling model of arterial walls. Journal of the Mechanics and Physics of Solids 153, 104498.

Humphrey, J., Rajagopal, K., 2002. A constrained mixture model for growth and remodeling of soft tissues. Mathematical models and methods in applied sciences 12, 407–430.

Khosravi, R., Miller, K.S., Best, C.A., Shih, Y.C., Lee, Y.U., Yi, T., Shinoka, T., Breuer, C.K., Humphrey, J.D., 2015. Biomechanical diversity despite mechanobiological stability in tissue engineered vascular grafts two years post-implantation. Tissue Engineering Part A 21, 1529–1538.

Lamm, L., Holthusen, H., Brepols, T., Jockenhövel, S., Reese, S., 2022. A macroscopic approach for stress-driven anisotropic growth in bioengineered soft tissues. Biomechanics and Modeling in Mechanobiology 21, 627–645.

Latorre, M., Humphrey, J.D., 2018. A mechanobiologically equilibrated constrained mixture model for growth and remodeling of soft tissues. ZAMM-Journal of Applied Mathematics and Mechanics/Zeitschrift für Angewandte Mathematik und Mechanik 98, 2048–2071.

Latorre, M., Humphrey, J.D., 2020a. Fast, rate-independent, finite element implementation of a 3d constrained mixture model of soft tissue growth and remodeling. Computer methods in applied mechanics and engineering 368, 113156.

Latorre, M., Humphrey, J.D., 2020b. Numerical knockouts–in silico assessment of factors predisposing to thoracic aortic aneurysms. PLoS computational biology 16, e1008273.

Latorre, M., Montans, F.J., 2018. A new class of plastic flow evolution equations for anisotropic multiplicative elastoplasticity based on the notion of a corrector elastic strain rate. Applied Mathematical Modelling 55, 716–740.

Latorre, M., Szafron, J.M., Ramachandra, A.B., Humphrey, J.D., 2022. In vivo development of tissue engineered vascular grafts: a fluid-solid-growth model. Biomechanics and Modeling in Mechanobiology , 1–22.

Loerakker, S., Ristori, T., 2020. Computational modeling for cardiovascular tissue engineering: the importance of including cell behavior in growth and remodeling algorithms. Current Opinion in Biomedical Engineering 15, 1–9.

Lou, Y., Yoon, J.W., 2017. J2-j3 based anisotropic yield function under spatial loading. Procedia engineering 207, 233–238.

Miehe, C., 1996. Numerical computation of algorithmic (consistent) tangent moduli in large-strain computational inelasticity. Computer methods in applied mechanics and engineering 134, 223–240.

Miller, K.S., Khosravi, R., Breuer, C.K., Humphrey, J.D., 2015. A hypothesis-driven parametric study of effects of polymeric scaffold properties on tissue engineered neovessel formation. Acta biomaterialia 11, 283–294.

Mousavi, S.J., Avril, S., 2017. Patient-specific stress analyses in the ascending thoracic aorta using a finite-element implementation of the constrained mixture theory. Biomechanics and modeling in mechanobiology 16, 1765–1777.

Mousavi, S.J., Farzaneh, S., Avril, S., 2019. Patient-specific predictions of aneurysm growth and remodeling in the ascending thoracic aorta using the homogenized constrained mixture model. Biomechanics and modeling in mechanobiology 18, 1895–1913.

Ramachandra, A.B., Humphrey, J.D., Marsden, A.L., 2017. Gradual loading ameliorates maladaptation in computational simulations of vein graft growth and remodelling. Journal of The Royal Society Interface 14, 20160995.

Ramachandra, A.B., Sankaran, S., Humphrey, J.D., Marsden, A.L., 2015. Computational simulation of the adaptive capacity of vein grafts in response to increased pressure. Journal of biomechanical engineering 137.

Simo, J.C., 1992. Algorithms for static and dynamic multiplicative plasticity that preserve the classical return mapping schemes of the infinitesimal theory. Computer Methods in Applied Mechanics and Engineering 99, 61–112.

Soleimani, M., 2019. Finite strain visco-elastic growth driven by nutrient diffusion: theory, fem implementation and an application to the biofilm growth. Computational Mechanics 64, 1289–1301.

de Souza Neto, E.A., Peric, D., Owen, D.R., 2011. Computational methods for plasticity: theory and applications. John Wiley & Sons.

Szafron, J.M., Ramachandra, A.B., Breuer, C.K., Marsden, A.L., Humphrey, J.D., 2019. Optimization of tissue-engineered vascular graft design using computational modeling. Tissue Engineering Part C: Methods 25, 561–570.

Valentin, A., Cardamone, L., Baek, S., Humphrey, J., 2009. Complementary vasoactivity and matrix remodelling in arterial adaptations to altered flow and pressure. Journal of The Royal Society Interface 6, 293–306.

Vignes, C., Papadopoulos, P., 2010. Material growth in thermoelastic continua: Theory, algorithmics, and simulation. Computer methods in applied mechanics and engineering 199, 979–996.

Vladimirov, I.N., Pietryga, M.P., Reese, S., 2008. On the modelling of non-linear kinematic hardening at finite strains with application to springback—comparison of time integration algorithms. International Journal for Numerical Methods in Engineering 75, 1–28.

Watton, P., Hill, N., Heil, M., 2004. A mathematical model for the growth of the abdominal aortic aneurysm. Biomechanics and modeling in mechanobiology 3, 98–113.

Yamakawa, Y., Hashiguchi, K., Sasaki, T., Higuchi, M., Sato, K., Kawai, T., Machishima, T., Iguchi, T., 2021. Anisotropic subloading surface cam-clay plasticity model with rotational hardening:

Deformation gradient-based formulation for finite strain. International Journal for Numerical and Analytical Methods in Geomechanics 45, 2321–2370.